Gondwana Research 149 (2026) 17–43

Contents lists available at ScienceDirect

Gondwana Research

journal homepage: www.elsevier.com/locate/gr

Birth, life and death of the Devonian Chaitenia back-arc along the Southwestern Gondwanan margin (southern Chile)

Gaëlle Plissart [a,*], Juan Carlos Moral Yilorm [b], José María González-Jiménez [c], Jesús Muñoz-Montecinos [d], Carolina Pavez Salgado [e], Aníbal Rivera Herrera [e], Fiona Cabrera Bermúdez [e], Claudio Marchesi [c,f], Alexandre Corgne [a], Antonio Jesús Moreno Abril [f], Pierre Lanari [g], Julien Berger [h], Alison Halton [i]

[a] Instituto de Ciencias de la Tierra, Universidad Austral de Chile, Casilla 567, Valdivia, Chile
[b] Departamento de Ciencias de la Tierra, Universidad de Concepción, Barrio Universitario s/n, Concepción, Chile
[c] Instituto Andaluz de Ciencias de la Tierra (IACT-CSIC), Avda. de las Palmeras 4, Armilla, Granada 18100, Spain
[d] Institute of Geology, Department of Earth and Planetary Sciences, ETH Zürich, Sonneggstrasse 5, 8092 Zurich, Switzerland
[e] Escuela de Geología, Universidad Austral de Chile, Casilla 567, Valdivia, Chile
[f] Departamento de Mineralogía y Petrología, Universidad de Granada, Avenida Fuentenueva s/n, 18002 Granada, Spain
[g] Institute of Earth Sciences, University of Lausanne, Géopolis CH-1050 Lausanne, Switzerland
[h] Géosciences Environnement Toulouse, Université de Toulouse, CNRS, CNES, IRD, UPS, 31400 Toulouse, France
[i] The Open University, Walton Hall, Milton Keynes, MK7 6AA, UK

ARTICLE INFO

Keywords:
Garnet-bearing amphibolites
Blueschists
Subduction
Chaitenia arc and back-arc
Chilenia collision

ABSTRACT

The late Paleozoic evolution of SW Gondwana at the current latitudes of 38-40°S involved three different blocks (Chilenia, Chaitenia and North Patagonia), whose origin and tectonic evolution is debated, making paleogeographic reconstructions challenging. Here we address this issue by constraining the tectonic setting and the metamorphic evolution of mafic rocks outcropping in three sectors (Guzmán at 38°33′S, San Carlos at 40°54′S, Los Pabilos at 40°57′S) of the late Paleozoic basal accretionary complex of the Chilean Coastal Cordillera. The geochemical results suggest that their protoliths originated in a back-arc lithosphere correlating with the Chaitenia back-arc while our *P–T–t* paths reconstructions show that this basin closed diachronically. In the southern part of the basin, the peak metamorphic conditions of ~ 450 °C and 1.4–1.6 GPa estimated for the San Carlos blueschists are interpreted as representing a cold thermal configuration for the subduction already reached at 335 Ma (*in situ* $^{40}Ar/^{39}Ar$ on phengite). Comparatively, in its northern part, the Guzmán garnet-bearing amphibolites still followed at the same time a warmer counterclockwise *P–T* path, interpreted as the initiation of the intra-back-arc subduction, reaching metamorphic peak conditions of ~ 650 °C and 1–1.2 GPa. The amphibolites further cooled down to 500 °C at 311–299 Ma (*in situ* $^{40}Ar/^{39}Ar$ on hornblende) and underwent a hydration event under conditions of 480–520 °C and 0.8–1.1 GPa at 277–270 Ma (*in situ* $^{40}Ar/^{39}Ar$ on actinolite). Our results suggest that the Chaitenia oceanic arc and back-arc system extended about 300 km further north than previously thought, up to the present 38°S latitude. Moreover, we propose that the opening of the Chaitenia back-arc is closely linked to along-strike transition from collision of the Chilenia terrane at the northwest to normal subduction beneath the North Patagonian margin at the southeast, triggering slab curving, tearing and roll-back.

1. Introduction

Oceanic back-arc basins (BAB) are seafloor spreading centers located in the hanging wall of subduction zones. Their formation is generally closely linked to subduction mechanisms (slab roll-back, landwards displacement of the overriding plate, strong mantle corner flow, strong asthenospheric flow due to slab break-off, toroidal flow at slab edges) (Artemieva, 2023 and references therein). It also depends on other external factors such as the age of the subducting plate or the strength of the overriding plate. However, other tectonic mechanisms that do not

* Corresponding author.
E-mail address: gaelle.plissart@uach.cl (G. Plissart).

https://doi.org/10.1016/j.gr.2025.07.023
Received 3 February 2025; Received in revised form 15 July 2025; Accepted 30 July 2025
Available online 18 August 2025

only involve subduction were also suggested like the pull-apart model (Jolivet et al., 1994), the extrusion of the overriding plate due to collision with a rigid terrane (Tapponnier, 1977; Mantovani et al., 2001), or the rotation of the fore-arc due to collision with buoyant crustal masses present in the subducting plate (Wallace et al., 2005; Magni et al., 2014).

Recent studies on the North Patagonian Massif have suggested the existence during the Devonian of a back-arc basin along the SW Gondwanan margin, referred to as the Chaitenia BAB (Rapela et al., 2021). However, its paleo-extension and the possible mechanisms for its formation are still unknown. Also, although the present South American basement between 27 and 47°S has been classically interpreted as a collage of several tectonic blocks onto the SW Gondwanan margin during the Paleozoic (Ramos et al., 1986; Willner et al., 2011; Hyppolito et al., 2014a), the recognized back-arc zone is located near the boundaries between three different micro-blocks (Chilenia, Chaitenia and North Patagonia; Fig. 1) whose provenance, evolution and limits are still unclear, hampering accurate geodynamic reconstructions (Pankhurst et al., 2006).

The Chilenia terrane (Fig. 1), with Laurentian affinity, would have collided at ca. 385 Ma onto a margin interpreted as already composed of the Cuyania accreted terrane (e.g. Ramos et al., 1986). However, the vergence of closure of the oceanic basin between both terranes is still controversial, with subduction dipping either to the actual east (Willner et al., 2011; Hyppolito et al., 2014a) or west (Davis et al., 2000; Cingolani and Ramos, 2017; Pérez Luján et al., 2021). Chilenia is thought to extend southwards to 37-39°S latitudes. Further south, the basement would correspond to the Patagonia block, whose evolution is still debated: this block is either viewed as resulting from two separated terranes (Fig. 1), the North Patagonian Massif and the Southern Patagonia-Deseado Massif (Pankhurst et al., 2006), or as a unique Patagonia terrane (Ramos, 2008). In the first case, the North Patagonian Massif is considered as an autochthonous/parautochthonous proto-Gondwanan entity since Siluro-Devonian (Pankhurst et al., 2006; 2014) or Cambro-Ordovician times (Rapela and Pankhurst, 2020; Rapalini et al., 2013). The Southern Patagonia (or the unique Patagonia terrane) is generally considered by the different authors to be allochthonous to Gondwana and accreted during the Carboniferous. It could also be considered as parautochthonous on a larger scale, being derived from the same proto-Gondwanan southern margin of the Rodinia supercontinent, as evidenced by a pre-Cambrian evolution similar to that of southeast Africa (Pankhurst et al., 2006; Ramos, 2008; Schilling et al., 2017).

The limit between North Patagonia and proto-Gondwana would correspond to the Huincul fault zone (HFZ, Fig. 1), where a marked WNW-ESE crustal discontinuity, as inferred from geophysical data at ca. 39°S, truncates the N-S trends of the Pampia-Cuyania-Chilenia structures (Kostadinoff et al., 2005; Mosquera and Ramos, 2006). An early to middle Permian transpressional deformation has been suggested at the north of the Patagonian Massif, based on the Permian Yaminué granitic complex deformed at high temperatures (Ramos, 2008; Pankhurst et al., 2014). This transpressional event does not display evidence for oceanic basin closure and could correspond to the first movements of the HFZ. In Chile, the continuation of this fault, and thus, the possible southern limit of Chilenia is unconstrained, and would pass north of Temuco (Ramos, 2008). Some authors interpreted its continuation as the WNW-ESE-striking Mocha-Villarica fault zone (MVFZ, Fig. 1; Romero et al., 2019), whereas others as the NW-SE-striking Lanalhue fault (LFZ, Fig. 1; Palape et al., 2022). The Lanalhue fault, which is recognized as a major and repeatedly activated crustal fault zone, displaced the Chilean Western and Eastern Series in a sinistral sense of shear during the early Permian (Glodny et al., 2008).

Based on O and Hf isotopes on Devonian zircons from granitic intrusions and metasedimentary rocks of the southern Chile accretionary complex, the Chaitenia block was recognized by Hervé et al. (2016) and Hervé et al. (2018) as a Devonian, oceanic island arc preserved on the western side of the Andes at the latitudes of the North Patagonian

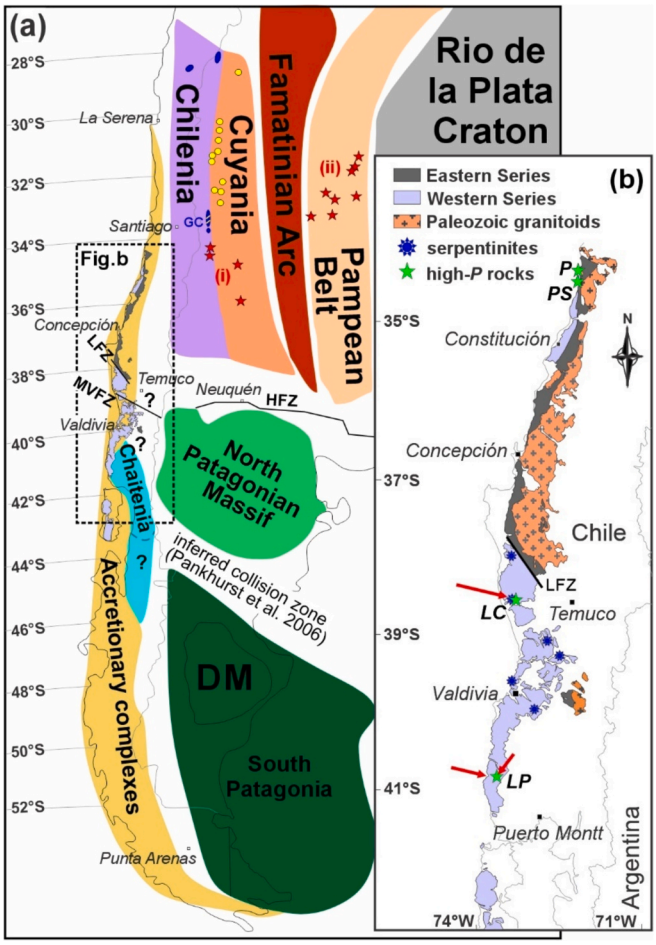

Fig. 1. **(a)** Map of South America showing the inferred location of the main tectonic blocks discussed in the text. Modified from Pankhurst et al. (2006), Pankhurst et al. (2014) and Hervé et al. (2018). DM: Deseado Massif; HFZ: Huincul Fault Zone; LFZ: Lanalhue Fault Zone; MVFZ: Mocha-Villarica Fault Zone. HFZ trace from Gregori et al. (2008). Eastern and Western Series from Hervé et al. (2013). The main lithological evidences for the Chilenia collision are indicated (yellow circles not to scale as the mafic belt from Boedo et al. (2021), deep blue ellipses as the possible outcrops of the Chilenia basement, including the Guarguaráz Complex (GC) as part of the mafic belt, Devonian granites of group (i) and group (ii) from Dahlquist et al. (2021) as red stars not to scale. **(b)** Zoom on the Western and Eastern Series and location of the three study sectors with red arrows (modified from Hervé et al. (2013) and Plissart et al. (2019)). The principal ultramafic bodies inside the Western Series are indicated, as well as recognized high-P rocks (P: Pichilemu blueschists, PS: Punta Sirena amphibolites and Grt-bearing micaschists, LC: La Cabaña olivine-bearing antigoritites, LP: Los Pabilos *retro*-eclogites). (For interpretation of the references to colour in this figure legend, the reader is referred to the web version of this article.)

Massif. It would have formed by the fore-arc rifting of a Devonian ca. 405–395 Ma continental arc due to slab roll-back. Rapela et al. (2021; 2024) proposed that this evolution led to the opening of the Chaitenia back-arc at 395–380 Ma, well defined at the 41-43°S latitudes (Fig. 1). This back-arc basin would have rapidly closed during the Carboniferous (380–340 Ma) due to the incoming and subsequent collision of the Chaitenia oceanic arc with the same North Patagonian Massif margin from which it previously rifted (Hervé et al., 2016; Hervé et al., 2018; Rapela et al., 2021; Palape et al., 2022). Although the Chaitenia block would have been located south of Chilenia, its northern limit has not yet been established. However, there is some evidence that Chaitenia may have extended as far as 38°33′S (Rapela et al., 2021). For example, detrital zircons of Devonian age (365–380 Ma) have been reported in the

enclosing metasedimentary schists of the La Cabaña ultramafic massif (38°33′S – 73°17′W), possibly derived from an island arc that developed to the west of the continental paleo-margin (Romero et al., 2017). In addition, the same ultramafic massif contains high-Cr chromitites typical of suprasubduction zone settings (González-Jiménez et al., 2014), in agreement with the presence of an oceanic arc/back-arc system in these latitudes.

To elucidate the tectonic configuration and evolution of this portion of the SW Gondwanan margin, the present study focuses on the tectonic origin and metamorphic evolution of meta-mafic rocks from the basal accretionary sequences outcropping (1) near the La Cabaña ultramafic massif in the Guzmán area, (2) in the sector of San Carlos-Manquemapu, and (3) in the Los Pabilos zone (Fig. 1b). We report the first occurrence of garnet-bearing amphibolites and fresh blueschists in the first and second localities, respectively. A detailed petrographic study was performed and coupled with mineral chemistry to unravel the paragenetic sequences preserved in the rocks. Conventional geothermobarometry, forward thermodynamic calculations and amphibole and phengite *in situ* $^{40}Ar/^{39}Ar$ dating were used to constrain *P–T–t* paths. Major and trace elements analyses of 40 samples from the three sectors allowed us to constrain the tectonic setting for the formation of the mafic protoliths. We discuss these results in the light of current tectonic knowledge and integrate them into a new large-scale paleogeographic model for the SW Gondwanan margin from Devonian to Permian time, including a possible mechanism for the formation of the Chaitenia back-arc complex.

2. Geological setting

2.1. Regional context

The metamorphic basement of the Chilean Coastal Cordillera (30° – 42°S) is divided into two geological units (Fig. 1b): the Eastern Series (LT-LP, locally HT) and the Western Series (LT-HP) (Hervé, 1988). The Eastern Series predominantly presents lithologies of metaturbidites, whose protoliths correspond to post-Devonian trench-filling sediments (Hervé, 1988). These rocks were affected by contact metamorphism under conditions of 400 to 720 °C and 0.25 to 0.35 GPa (Willner et al., 2005) during the emplacement of the Coastal Batholith between 296 and 305 Ma (Willner et al., 2005; Deckart et al., 2014). The Western Series presents intercalations of metaturbidites, quartzites, meta-mafic rocks, metacherts, serpentinized peridotites, Fe-Mn rich metasediments, and rare sulfide mineralizations, resulting from accretion and underplating at the base of the late Paleozoic accretionary prism (Glodny et al., 2005; Willner et al., 2005). The meta-mafic rocks studied here from Guzmán, San Carlos-Manquemapu and Los Pabilos belong to the Western Series (Fig. 1b).

Between 30 and 36°S, the meta-mafic rocks incorporated in the Western Series display a variety of geochemical signatures such as E-MORB, OIB and N-MORB, interpreted as the basal accretion of mafic material from the slab whose protoliths formed either at a mid-oceanic ridge, near a continental break-up zone associated to a plume, at a plume-influenced ridge or in the seamount itself (Hyppolito et al., 2014a; Muñoz-Montecinos et al., 2024). South of these latitudes, the geotectonic setting for the formation of the mafic protoliths is unconstrained.

The Western Series can be divided into a northern (34-36°S) and a southern sector (38-43°S), separated by the Lanalhue Fault (Fig. 1b). In both sectors, previous estimations of *P–T* conditions recorded *P–T* metamorphic paths that are both clockwise and counterclockwise. In the northern sector of the Western Series, regional high-pressure conditions of 0.7–0.9 GPa and 380–420 °C characteristic of the base of the prism have been determined for the interlayered metasedimentary and meta-mafic sequence at 292–308 Ma, and a later retrogression occurred at 0.4–0.7 GPa and 300–380 °C over a period extending 30 to 40 Ma after the metamorphic peak (Willner, 2005; Willner et al., 2005). In the Pichilemu area (34°23′S, Fig. 1b), blueschists recorded *P–T* conditions between 0.8–1.1 GPa and 380–420 °C at 291–308 Ma, with a retrograde overprinting under greenschist facies conditions of 0.4–0.8 GPa and 300–360 °C (Willner, 2005; Halama and Konrad-Schmolke, 2015; Muñoz-Montecinos et al., 2020). In Punta Sirena (34°32′S, Fig. 1b), garnet-bearing micaschists and amphibolites recorded peak metamorphic conditions of 1.25–1.4 GPa/540–580 °C and 0.95–1.0 GPa/540–575 °C respectively, at ca. 335–330 Ma, followed by an isobaric cooling (Hyppolito et al., 2014b). Both lithologies would have been incorporated in the base of the prism at 308 Ma (Hyppolito et al., 2014b). These amphibolite facies *P–T* conditions and the reconstructed counterclockwise trajectory are interpreted as linked to the initial stages of subduction when the hanging mantle was still warm (Willner, 2005; Hyppolito et al., 2014b).

In the southern sector, the Western Series was defined by Duhart et al. (2001) as the Bahia Mansa Metamorphic Complex (39°30′-42°00′S), with the presence of pelitic and semi-pelitic rocks, metasandstones, metacherts, meta-mafic rocks and meta-ultramafic rocks (Barra et al., 1998; Duhart et al., 2001; Höfer et al., 2001). The regional *P–T* conditions recorded in this sector suggest mainly high-*P* greenschist transitional to blueschist facies conditions (0.8–0.9 GPa and 420 °C), at 260–220 Ma (Duhart et al., 2001; Glodny et al., 2005). However, in the Los Pabilos sector (~41°S, Fig. 1b), boulders of garnet-bearing amphibolites (1.1–1.65 GPa and 600–760 °C) and *retro*-eclogites (> 1.3 GPa and ~ 550 °C) recorded higher pressure conditions at 361 Ma and retrogression to blueschist facies conditions at 325 Ma (1.0–1.4 GPa and 350–500 °C; Willner et al., 2004; Kato et al., 2008). This counterclockwise *P–T* trajectory is interpreted as resulting from material incorporation in the subduction channel at the beginning of the subduction.

2.2. Geology of the Guzmán sector

The sector of Guzmán is located near the well-studied ultramafic complex of La Cabaña in the Araucania Region (38°33′S – 73°17′W) (Fig. 2a). Two principal outcrops of 1 to 4 km^2 of serpentinized ultramafic bodies are intercalated within meta-mafic and metasedimentary rocks (Barra et al., 1998; Höfer et al., 2001). These ultramafic bodies display variably serpentinized dunite, harzburgite and wehrlite protoliths possibly linked to the mantle wedge (Plissart et al., 2019), including rare chromitites and Platinum-Group Minerals (González-Jiménez et al., 2014; 2016; 2021). Previous works on the La Cabaña ultramafic mantle rocks suggested that they originally formed in a context of suprasubduction, but the tectonic environment is still not well constrained, varying from fore-arc, back-arc (Frutos and Alfaro, 1987; Höfer et al., 2001; Plissart et al., 2019) or intra-arc (Barra et al., 1998; González-Jiménez et al., 2016) position. Bulk-rock geochemical data of the ultramafic rocks display patterns similar to those of mantle wedge serpentinites (González-Jiménez et al., 2016), consistently with high-Cr and Os-Ir-Ru enrichment over Pt-Pd in the associated chromitite ores (González-Jiménez et al., 2014). The tectono-metamorphic evolution undergone by these rocks has been recently detailed in Plissart et al. (2019). Mylonitic antigorite schists recorded *P–T* conditions of 1.1 GPa and ~ 600 °C for an assemblage composed of metamorphic olivine + antigorite + magnetite + dolomite. Such conditions suggest that these rocks were captured by the serpentinitic subduction channel along a hot *P–T* path, when the subduction system was still thermally immature. Additionally, González-Jiménez et al. (2017) reported evidence of the presence of a higher-pressure assemblage composed of antigorite + metamorphic olivine + Ti-clinohumite + Ti-chondrodite + magnetite, for which they estimated equilibrium conditions of 1.5–2.5 GPa (> 50 km) for 450–650 °C. Such conditions would prevail along a cold *P–T* path, when the subduction system was already thermally mature. The tectonic incorporation of the ultramafic bodies inside the metasediments has been dated at 282 ± 6 Ma by K-Ar in fuchsite from adjacent metasediments, interpreted as crystallizing from ultramafic-derived Cr fluids

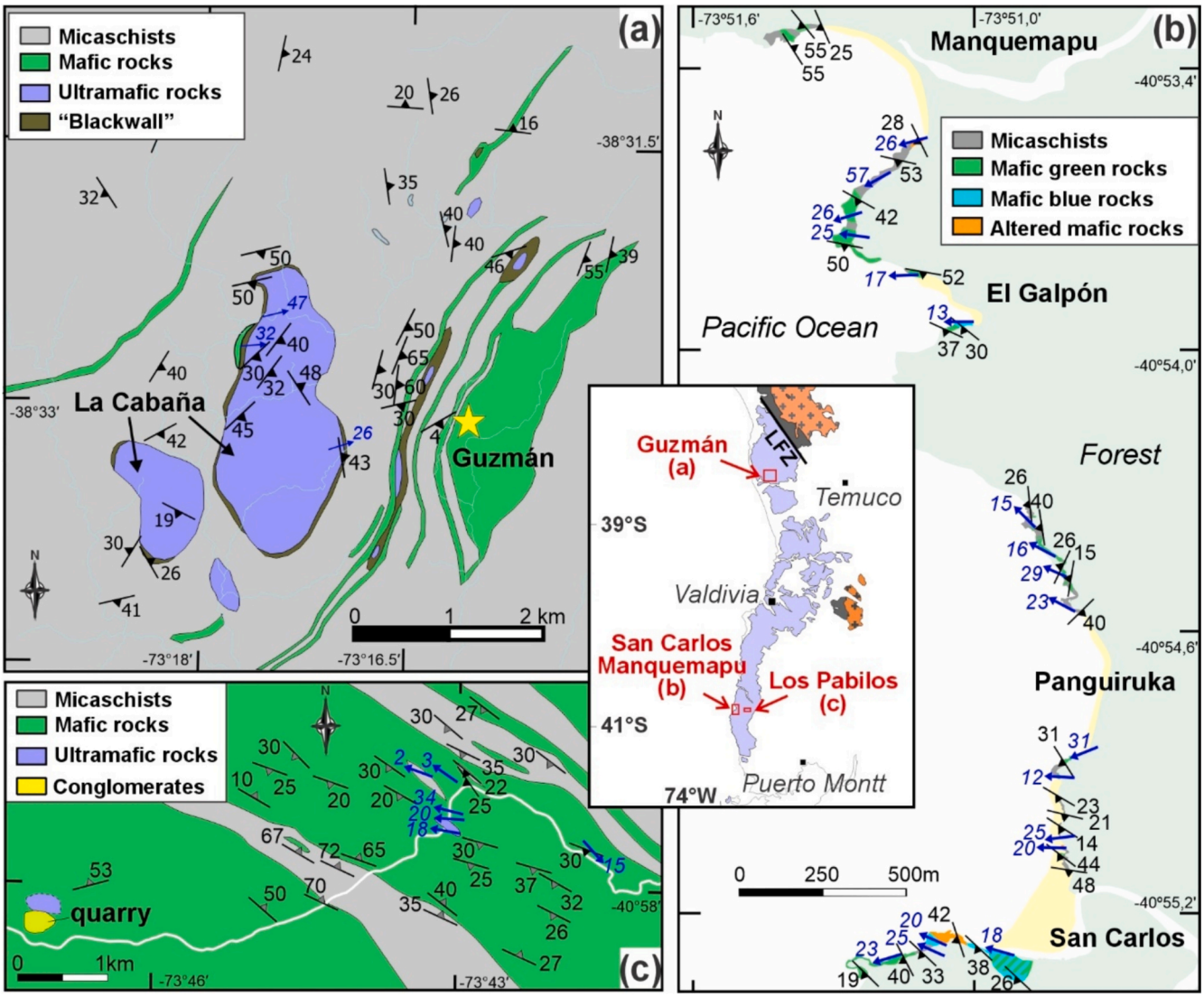

Fig. 2. Geological maps of the three sectors studied. **(a)** Guzmán sector (yellow star), modified from Höfer et al. (2001) and Plissart et al. (2019), showing the mafic rocks outcropping near the ultramafic bodies of La Cabaña. Representative S2 foliations in micaschists and ultramafic rocks are shown, as well as L1 lineations in the mylonitic serpentinites. For a detailed structural map, see Plissart et al. (2019). **(b)** San Carlos-Manquemapu sector, showing mafic rocks interspersed with micaschists, as well as representative L1 lineations and S1 foliations in mafic rocks and S1//S2 in micaschists. Note the occurrence of blueschists in San Carlos and El Galpón. **(c)** Los Pabilos sector, showing the boulders quarry location and new mapping 5 km at the east. Representative S1 and L1 mylonitic foliations are shown as well as previous measurements (grey symbols) from Kato et al. (2008). (For interpretation of the references to colour in this figure legend, the reader is referred to the web version of this article.)

(Höfer et al., 2001) and at ~ 283.4 ± 7 Ma by U-Pb SHRIMP on zircons from the metasomatic reaction zone or '*blackwall*' that formed between the ultramafic body and the metasediments once they juxtaposed (Romero et al., 2017).

Apart from the ultramafic bodies, large strips and zones of mafic rocks such as the Guzmán sector crop out in the La Cabaña area (Fig. 2a). They consist of green schists and more massive meta-mafic rocks, whose origin is poorly constrained. Höfer et al. (2001) described them as metavolcanic rocks with paragenesis of albite + actinolite + chlorite + titanite + epidote + clinozoisite + quartz ± biotite ± magnetite, which would possibly derive from pyroclastic rocks or basaltic sills intruding the sediments (Höfer et al., 2001). Our structural data indicate that the mafic schists display the same orientation as the metasedimentary micaschists defining the regional S2 foliation (N021/23E) (Plissart et al., 2019) (Fig. 2a). In addition, more massive mafic blocks are embedded as lenses within micaschists, with similar internal foliation. Moreover, we discovered garnet-bearing amphibolites as boulders in the Guzmán area.

2.3. Geology of the San Carlos-Manquemapu sector

This study presents the first detailed lithological and structural characterizations of the San Carlos–Manquemapu area (40°55′S, 73°51′W), located in the Los Lagos Region (Fig. 2b). Our mapping shows that the meta-mafic rocks and metasediments are distributed in all the beaches, interspersed at various scales (decametric layers to 300 m-wide zones) (Fig. 2b). The pelitic rocks are mainly composed of albite-bearing graphitic schists with intrafolial quartz lenses. The mafic rocks commonly consist of mylonitic albite-bearing greenschists hosting stretched epidote-rich lenses. Blueschists were found in two sectors: San Carlos and El Galpón (Fig. 2b). The blueschists (coarse glaucophane + epidote ± white micas) occur in two forms: (i) decimetric to metric boudins or centimetric to decimetric layers with sharp contacts, embedded into (ii) blue-green schists, displaying blueish to greenish gradational zones. In San Carlos, the blue-green zone crops out in a 50 m-wide band parallel to the stretching lineation and is possibly wider if correlated with isolated outcrops nearby. In the El Galpón area, the blue-

green zone is smaller, only 10 m-wide parallel to the stretching lineation. Finally, relict of glaucophane has been encountered in various samples in Panguiruka. The mafic schists (green, blue-green and blue) display a S1 mylonitic foliation gently dipping to the SW (average N133/31 W). The associated L1 stretching lineation plunges consistently to the WNW (average N277/21) (Fig. 2b). Asymmetric lenses, boudins and porphyroclasts indicate that the D1 deformation corresponds to a subhorizontal simple shear. The metapelites show a S2//S1 foliation, originating from axial planes of recumbent crenulation, dipping to the SW (average N143/26SW), as well as some stretching lineations preserved in quartz lenses and curtain folds plunging more variously towards the NW, W or SW (average N281/34).

2.4. Geology of the Los Pabilos sector

The area of Los Pabilos (40°58′S – 73°46.5′W) is located in the Coastal Cordillera in the Los Lagos Region (Fig. 2c). Previous studies in this sector reported the occurrence of *retro*-eclogites, *retro*-amphibolites, serpentinites and garnet-bearing micaschists as boulders near a serpentinitic body (e.g. see Willner et al., 2004; Kato et al., 2008 for more details). These authors estimated peak *P–T* conditions for the garnet-bearing *retro*-amphibolite and *retro*-eclogite assemblages of 1.1–1.65 GPa and 600–760 °C and > 1.3 GPa and ~ 550 °C, respectively. A blueschist-facies overprint is estimated at 1.0–1.4 GPa and 350–500 °C. $^{40}Ar/^{39}Ar$ hornblende plateau age for a *retro*-amphibolite yielded 361 ± 1.7 Ma, interpreted as a minimum age for the metamorphic peak, whereas $^{40}Ar/^{39}Ar$ white mica plateau age gave 325 ± 1.1 Ma, interpreted as the age of the blueschist-facies overprint (Kato et al., 2008).

We have collected (from quarry boulders) an even greater diversity of lithologies including foliated garnet-bearing and garnet-free blueschists, massive metagabbroic rocks, garnet-bearing and garnet-free fine to coarse-grained amphibolites, metabasalts with doleritic texture, flaser gabbro (with and without garnet) and variably strained serpentinites. We also mapped a new small sector in Cuesta Brava at 5 km east of the quarry (Fig. 2c, 40°57′S – 73°43′W) where we found a 30 m-long serpentinitic body embedded inside mylonitic meta-mafic rocks (greenschists, metabasalts, metagabbros). These meta-mafic rocks display a S1 subhorizontal mylonitic foliation and associated strong L1 stretching lineation (average N291/16 W).

3. Methodology

We mapped and selected 40 mafic rocks sampled from the three sectors (Appendix 1): (i) Guzmán (Fig. 2a), (ii) San Carlos-Manquemapu (Fig. 2b) and (iii) Los Pabilos (Fig. 2c). All these samples have been carefully studied under optical microscope and were chosen in order to represent the lithological diversity of each sector (Appendix 1). Petrographical description of these samples can be found in Appendix 2. For the Guzmán sector, two samples were selected for mineral chemistry and thermobarometry [GP-15-2C (retrogressed garnet-bearing amphibolite) and GP-15-3 (greenschist)] and one sample for *in situ* $^{40}Ar/^{39}Ar$ dating [GP-15-2C]. Similarly, for the San Carlos-Manquemapu sector, three samples [MA-18-72 (garnet-bearing blueschist), MA-18-77a (locally retrogressed blueschist), MA-18-67 (strongly retrogressed blueschist)] were selected for mineral chemistry and thermobarometry and one sample for *in situ* $^{40}Ar/^{39}Ar$ dating [MA-18-72]. For all the selected samples, we applied scanning electron microscope (SEM) at the Unidad de Microscopia Electronica (Universidad Austral de Chile) and electron probe microanalysis (EPMA) at the Raimond Castaing Center (Toulouse, France) including mapping (Appendix 3). For thermobarometry, we used empirical thermometers and barometers and we also performed isochemical phase diagrams using *Perple_X* (Connolly, 2009, version 7.1.6) together with the thermodynamic data from Holland and Powell (2011; *hp622ver.dat*) for minerals and fluid phase. Reactive bulk compositions were determined by micro-mapping obtained from compositional maps using the *XMapTools* 3.4.1 software (method described in Lanari and Engi, 2017). More details of the methodology used to calculate phase diagrams and solid solution models are found in Appendix 6. Furthermore, we performed whole-rock geochemical analyses on the 40 samples in the ALS Laboratory (Lima, Peru) and at the Instituto Andaluz de Ciencias de la Tierra (IACT, Granada, Spain) (Appendix 4). Finally, the GP-15-2c sample of garnet-bearing retrogressed amphibolite, as well as the MA-18–72 sample of garnet-bearing blueschist, were prepared respectively for amphibole and white mica *in situ* $^{40}Ar/^{39}Ar$ dating in polished sections, 200 μm in thickness at the Open University (UK). Tables of results can be found in Appendix 5. Full analytical details for all the performed analyses are provided in Appendix 6. Mineral abbreviations are from Warr (2021).

4. Results

4.1. Petrography and mineral chemistry

4.1.1. Sector of Guzmán

4.1.1.1. GP-15-2c retrogressed garnet-bearing amphibolite. The GP-15-2c retrogressed garnet-bearing amphibolite is made of approximatively 44 vol% of green amphibole, 41 % of epidote, 10 % of titanite, 3 % of garnet, 1 % of biotite and 1 % of rutile/ilmenite, defining a granonematoblastic texture (Fig. 3a). Prismatic amphiboles are up to 400 μm in length and display green–brown pleochroism in their core and pale green pleochroism in their rims (Fig. 3b,c). Amphiboles are mainly calcic, ranging from magnesio-ferro hornblende to actinolite, with Mg# (molar $Mg/(Mg + Fe^{2+})$) between 0.42 and 0.62 (Appendix 3). A clear chemical zoning exists between the core (Mg/Fe-hornblende) and the rims (actinolite) (Appendix 3). Interstitial chlorite is identified as daphnite-clinochlore (Mg# of 0.47–0.48, Appendix 3) whereas, when replacing amphibole (Fig. 3c), it displays a higher sudoite component (X_{Sud}: 0.04–0.09). Epidotes are elongated and 100–400 μm in length (Fig. 3a). They classify as epidote *sensu stricto* with $^{[M3]}XFe^{3+}$ = 0.63–0.73; Appendix 3), without significant chemical zoning. Amphibole and epidote define the main foliation, which contains dispersed titanite aggregates (Fig. 3a,c). No plagioclase is observed in these rocks. Garnet porphyroblasts (up to 1 mm in diameter) display brownish cores (Grt I) in transmitted light whereas the rims (Grt II) are translucent (Fig. 3b). Backscattered electron SEM imaging and EMPA mapping reveal the presence of three chemical zones within garnet (Fig. 3d, Fig. 4, Appendix 3): (i) an almandine-grossular Grt I inner core (mean X_{Alm}: 0.57; X_{Grs}: 0.24; X_{Prp}: 0.14; X_{Sps}: 0.05), (ii) a thin brighter intermediate zone (5–20 μm-thick) (mean X_{Alm}: 0.50; X_{Grs} 0.26; X_{Prp}: 0.04; X_{Sps}: 0.21), and (iii) an almandine-grossular-spessartine Grt II outer rim (mean X_{Alm}: 0.39; X_{Grs}: 0.40; X_{Prp}: 0.02; X_{Sps}: 0.19). The relict cores are chemically homogeneous although some have been nearly completely resorbed, resulting in very small preserved cores. The Grt II outer rims can be large and correspond to core replacement and possibly overgrowth as indicated by locally euhedral external borders. The chemical zoning is characterized by a decrease of Mg and Fe from the Grt I core towards the intermediate zone and towards the Grt II rims, an increase of Mn from the Grt I core towards both the intermediate zone and the rim with similar values, and an increase of Ca from the Grt I core and intermediate zone with similar values towards the rim (Fig. 4). This zoning is thus associated with almandine (prograde) and spessartine (retrograde) compositions, respectively. Oriented inclusion trails of small epidote are observed inside garnet cores (Fig. 3a,b) and are characterized by higher $^{[M3]}XFe^{3+}$ (0.71–0.73) than foliation-defining epidote (Appendix 3). Finally, rare blasts of biotite (up to 1 mm) with Mg# between 0.44 and 0.45, classified as annites *sensu lato* (X_{Phl}: 0.36–0.37; X_{Ann}: 0.44–0.47; X_{Eas}: 0.07–0.09; X_{Sid}: 0.09–0.11; Appendix 3), are dispersed in the matrix and probably correspond to the retrogression of garnet. Backscattered electron SEM imaging revealed that garnet cores contain inclusions of ilmenite and rutile up to 100 μm. Ilmenite is found

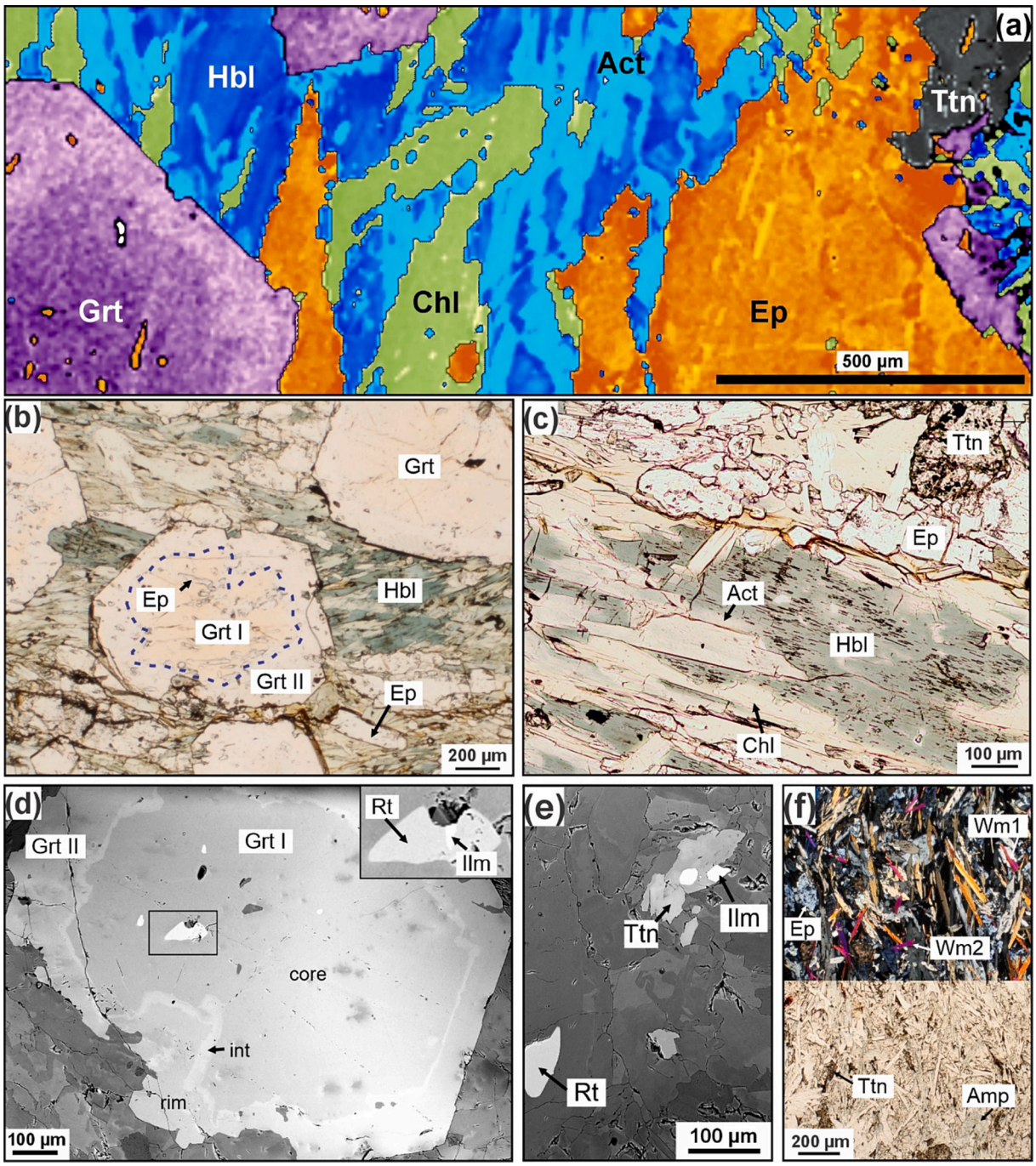

Fig. 3. Representative microscopic textures and mineral relationships in the Guzmán GP-15-2C retrogressed garnet-bearing amphibolite (a-e) and GP-15-3 greenschist (f). **(a)** Phase mask image constructed based on X-ray map of aluminum (unit: count), displaying textures and compositional features. **(b)** Brown zoning and small epidote inclusions in garnet cores (blue segmented lines). **(c)** Zoning in amphibole, displaying hornblende core and actinolite rims together with chlorite. **(d-f)** BSE images displaying a variety of microtextures and garnet zoning. **(d)** Garnet zoning displaying a core surrounded by a brighter intermediate zone and a rim whose width varies considerably. Note the inclusions of ilmenite surrounded by rutile within the garnet core. **(e)** Rutile and ilmenite in the matrix; destabilization of ilmenite into titanite. **(f)** White micas (WM1), epidotes (Ep) and amphiboles (Amp) sub-parallel to the foliation and white micas (WM2) isotropic respective to the foliation. (For interpretation of the references to colour in this figure legend, the reader is referred to the web version of this article.)

included within rutile (Fig. 3d), suggesting its possible transformation into the latter. Rutile is also included in garnet as a single phase. Rutile and ilmenite are also present in the matrix, as grains up to 100 µm (Fig. 3e,f). Ilmenite is commonly present as relict grains surrounded by titanite (Fig. 3e,f).

Consequently, the mineral parageneses proposed for this lithology consist of 1): Hbl + Ep/Pl (?) + Grt I (core) ± Ilm ± Rt for the metamorphic peak and 2): Act + Grt II (rim) + Chl + Ep + Ttn ± Bt for retrograde conditions.

4.1.1.2. GP-15-3 Greenschist. The GP-15-3 greenschist is made of approximately 39 vol% of green amphibole and chlorite, 35 % of epidote, 20 % of white mica and 6 % of titanite (Fig. 3f). It presents a well-developed foliation defining a lepidonematoblastic texture (Fig. 3f). Amphibole is prismatic, up to 300 µm in length and displays dark green hornblende cores and pale green actinolite rims (Fig. 3f).

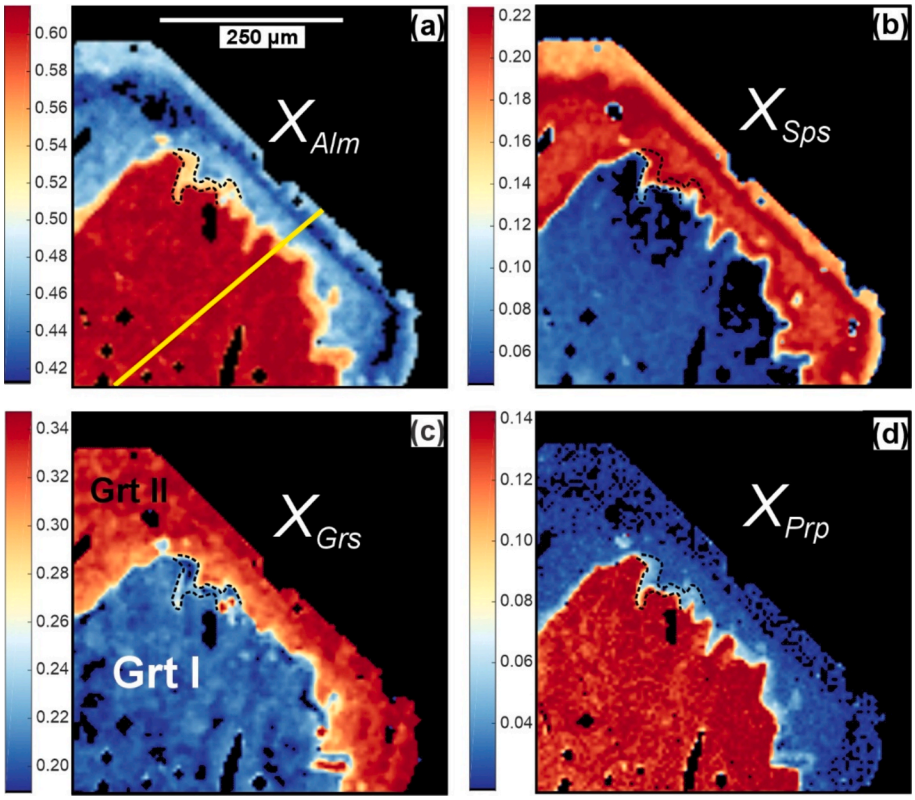

Fig. 4. Chemical map of garnet of the Guzmán GP-15-2C retrogressed garnet-bearing amphibolite showing the variation of the garnet endmembers X_{Alm}, X_{Sps}, X_{Grs}, X_{Prp} from core to rim. The bright intermediate zone is indicated with black dashes. See text for description. The location of the EMPA profile from Appendix 3 is shown in yellow. (For interpretation of the references to colour in this figure legend, the reader is referred to the web version of this article.)

Mg# varies between 0.63 and 0.74 (Appendix 3). Epidote is prismatic tabular and up to 200 µm in length. Chlorite shows clinochlore component with Mg# of 0.60–0.61 and occurs in the matrix or as pseudomorphic replacement of amphiboles. Accessory titanite is dispersed within the foliation and can contain minute relict grains of rutile. No plagioclase is observed. Besides, white mica with sizes between 50–200 µm is either oriented sub-parallel to the foliation (WM1) or disposed isotropically (WM2) (Fig. 3f), the latter being possibly produced by subsequent static recrystallization. Both WM generations are partially included within the actinolite and epidote rims, which suggests that their crystallization occurred during the growth of these minerals. WM1 and WM2 are phengitic in composition, displaying Si (apfu) and Mg# contents ranging from 3.24 to 3.45 and 0.64 to 0.72, respectively (Appendix 3), without noticeable chemical variations. Based on the observed textural relationships, the main paragenetic association for the greenschist corresponds to retrograde conditions and consists of Act + Chl + Ep + WM + Ttn.

4.1.2. Sector of San Carlos-Manquemapu

4.1.2.1. MA-18-72 Garnet-bearing blueschist. The MA-18-72 garnet-bearing blueschist is made of approximately 35 vol% of sodic amphibole, 40 % of white mica, 20 % of epidote, 5 % of garnet, and other minor phases such as titanite, chlorite, magnetite, quartz, actinolite and albite (Fig. 5). The main foliation is defined by coarse- to medium-grained laths of white mica along with oriented prisms of sodic-amphibole and epidote (Fig. 5a). A previous folded foliation (S1a) is preserved in some microlithon zones and the S1b axial plane folds are parallel to the main foliation (Fig. 5c-f, see also Appendix 5–2). White mica and sodic amphibole in folded microlithons are less stretched than the ones from the main foliation and white mica grains are also bigger. Garnet occurs as euhedral blasts up to 800 µm in size (Fig. 5) and is also found included in sodic amphibole together with epidote, both in S1b and folded S1a glaucophane (Fig. 5c-d). This suggests that garnet and sodic amphiboles were stable during the S1a formation and were further crenulated and stretched during the S1b simple shear event, as evidenced by glaucophane tails (Fig. 5). Glaucophane is also rarely encountered included in garnet and epidote. Epidote is frequently included inside garnet, and in addition to the elongated prisms defining the main foliation, it also occurs as tabular rounded larger blasts (diameter of 1 mm) producing white micas pressure shadows (Fig. 5b). Cm-large massive boudins of epidote ± white micas and of glaucophane + white micas are embedded in the main foliation (Fig. 5a). Rare rutile occurs as relict within titanite (Fig. 5h). Chlorite is clinochlore-daphnite (Appendix 3; Mg# of 0.48–0.54) and occurs as pseudomorphic replacement after garnet and in the matrix (Fig. 5g). Albite is locally observed as pressure shadows around sodic amphiboles (Fig. 5g).

Sodic amphibole is glaucophane to ferro-glaucophane, with Mg# varying between 0.41 and 0.61 (Appendix 3). Calculated Fe^{3+} contents range between 0.2 and 0.9 apfu. In S1a and big S1b grains, a weak chemical zoning pattern is characterized by cores showing slightly higher amounts of Ca and Mg and lower Na and Al contents than sodic rims, whereas such zoning is mainly lost in elongated grains (Fig. 6d,g). Moreover, tails display similar Na contents than the previously mentioned rims, but lower Mg#. Also, few winchite and actinolite grains occur as thin rims around sodic amphiboles (Fig. 6g, Appendix 3). White mica occurs in two main microstructural domains: folded WM1a in relict microlithons (Fig. 5c-f) and WM1b defining the main S1b foliation (Fig. 5). All of them display Si (apfu) contents ranging from 3.38 to 3.46 and XMg from 0.44 to 0.57 (Fig. 6h, Appendix 3) and classify as phengite (Deer et al., 2003). There are no major chemical variations between WM1a hinges and WM1b main foliation, except that WM1b displays slightly higher amount of Si respect to WM1a (Fig. 6h, Appendix 3). Garnet corresponds to almandine (mean X_{Alm}: 0.41–0.52; X_{Grs}:

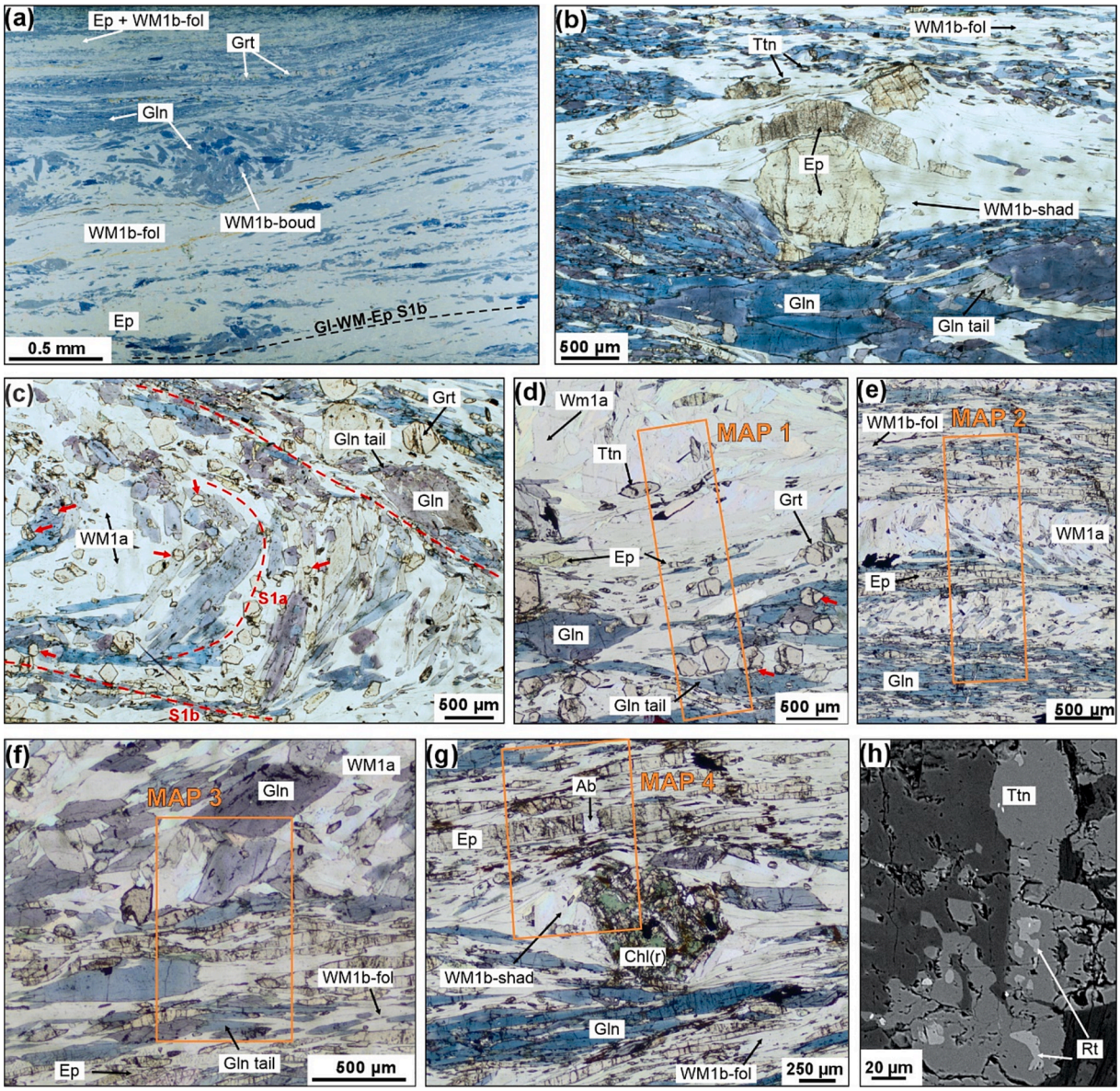

Fig. 5. Representative textures of the San Carlos-Manquemapu MA-18-72 garnet-bearing blueschist. **(a)** Simple shear foliation S1b made of glaucophane, epidote and white micas layers. WM1b-fol (foliation), WM1b-boud (inside boudin), WM1b-shad (in pressure shadows). **(b)** WM1b pressure shadows next to epidote blast. **(c)** Intrafolial folding of S1a whose axial plane defines the foliation S1b. Red arrows indicate garnet grains included in glaucophane inside the folded S1a. **(d-e-f)** Zooms of S1a microlithons and S1b cleavage zones and location of X-ray compositional maps 1, 2 and 3. **(g)** Retrograde zone (map 4) with chlorite replacing garnet and albite within epidote micro-boudin neck. **(h)** BSE image of rutile within titanite. (For interpretation of the references to colour in this figure legend, the reader is referred to the web version of this article.)

0.23–0.27; X_{Prp}: 0.02–0.03; X_{Sps}: 0.22–0.32, Appendix 3). Two growth stages can be distinguished (Fig. 6a-c): 1) the Grt 1 core, displaying from core to rim a decrease in Mn and increase in Fe, with constant Mg, and 2) the Grt 2 rim, displaying lower XMg and similar Mn and Fe contents to the internal core. This suggests that Grt 1 grew during a prograde path and reequilibrated or was overgrown by Grt 2 during a retrograde path. As Grt 2 is in textural equilibrium with glaucophane, epidote and white micas (Fig. 5, Fig. 6), this retrograde path likely occurred at high-*P*. Epidote corresponds to epidote *sensu stricto* with $^{[M3]}XFe^{3+} = 0.80–0.88$ (Appendix 3) and a zoning is observed between cores enriched in Fe and Mn and rims enriched in Al and poorer in Mn (Fig. 6f).

The observed textural relationships allow us to define the following stages for the garnet-bearing blueschist: 1) relict of a prograde path recorded in Ca-rich glaucophane + Fe^{3+}-epidote cores + growing garnet 1; 2a) metamorphic peak recorded by the S1 assemblage of glaucophane + Al^{3+}-epidote rims + white micas 1 + garnet 1 rims + titanite ± rutile; 2b) a high-*P* retrograde path with the same phases except garnet 2; and 3) local, low-*P* retrograde path (S2) with crystallization of actinolite, chlorite, albite and quartz.

4.1.2.2. MA-18-77a locally retrogressed blueschist. The sample MA-18-77a corresponds to a blueschist with local greenschist-facies retrogression localized within S2 bands (Fig. 7a). These are made of chlorite, albite (Appendix 3), white mica 2 and massive epidote and are subparallel to the glaucophane + epidote + white mica S1b foliation (Fig. 7b). Winchite and actinolite are frequent in the retrogression bands (Fig. 7), where glaucophane destabilized into albite, as well as in the rim of glaucophane near these bands. No garnet has been observed in this rock. No chemical differences have been observed between the different chlorite types. They classify as clinochlore with Mg# between 0.60 and 0.67 (Appendix 3). White micas from the main foliation (WM1) display Si (apfu) contents ranging from 3.39 to 3.50 while those in the

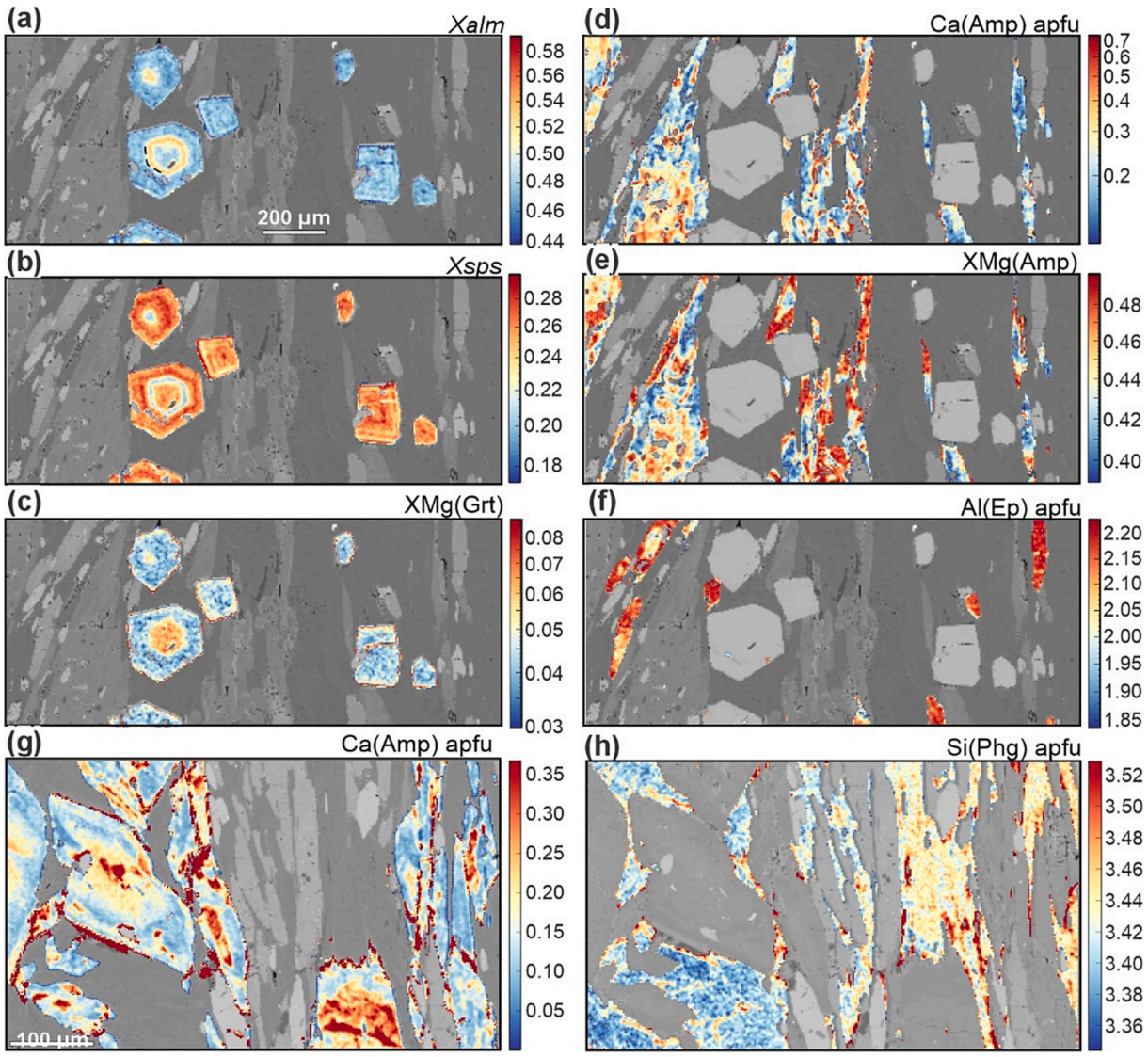

Fig. 6. Compositional maps of zone 1 **(a-f)** and zone 3 **(g-h)** of San Carlos-Manquemapu MA-18-72 garnet-bearing blueschist. See text for details.

retrograde bands (WM2) are globally lower from 3.40 to 3.45 (Appendix 3). Epidotes correspond to epidote *sensu stricto* with $^{[M3]}XFe^{3+}$ = 0.71–0.74 for the elongated S1b prisms, 0.67–1.00 for the grains near the retrobands and 0.70–0.93 for the massive grains inside the retrobands (Appendix 3).

4.1.2.3. MA-18-67 strongly retrogressed blueschist. The MA-18-67 sample displays a nearly complete retrogression to a chlorite, actinolite-winchite, epidote, pure albite and titanite mineral assemblage (Fig. 7c-e). Glaucophane is only present as inclusions in epidote blasts (Fig. 7e). C'-shear bands made of albite and actinolite (Fig. 7d) are associated to the retrogression event and we interpret the main foliation as corresponding to S2. Chlorite classifies as clinochlore-daphnite (Appendix 3), with Mg# of 0.47–0.59. Some bands of WM2 white micas are present, with Si(apfu) contents of 3.43–3.46. $^{[M3]}XFe^{3+}$ in epidote ranges from 0.71 to 1.00 (Appendix 3).

4.2. P–T estimates

4.2.1. Conventional geothermobarometry

4.2.1.1. Sector of Guzmán. For the metamorphic peak, we considered the Fe-Mg cationic exchange between garnet cores and hornblende preserved in the retrogressed garnet-bearing amphibolite GP-15-2C, using the thermometers of Graham and Powell (1984), Perchuk et al. (1985) and Ravna (2000). Detailed results are shown in Appendix 7 and yield averages between 645 and 735 °C. For pressure estimates, we used the Ernst and Liu (1998) semi-quantitative barometer based on Al_2O_3 contents in hornblende, considering a temperature of 650 °C, which yields 0.9 – 1.3 GPa (Appendix 7).

For the retrograde event, rims of garnet and biotite of the retrogressed garnet-bearing amphibolite GP-15-2C gave average temperatures of 452 °C – 502 °C (Kleemann and Reinhardt, 1994; Holdaway, 2000; Kaneko and Miyano, 2004) (Appendix 7). Chlorite thermometry (Cathelineau, 1988; Lanari et al., 2014) was also applied in this rock, giving retrograde temperatures between 368–281 °C and 568–271 °C for each calibration, as well as in the GP-15-3 greenschist, yielding ranges of 320–309 °C and 513–355 °C (Appendix 7). For the pressure estimates, we applied the Si-in-phengite barometer of Massonne and Schreyer (1987) and Kamzolkin et al. (2016) in the GP-15-3 greenschist. Results are shown in Appendix 7 and were calculated for a mean retrograde temperature of 475 °C. For the Massonne and Schreyer (1987) barometer, WM1 and WM2 give very similar pressure ranges of 0.89–1.15 GPa and 0.68–1.18 GPa, respectively, with averages of 1.02 and 1.00 GPa. The barometric results of the group 1 calibration of Kamzolkin et al.

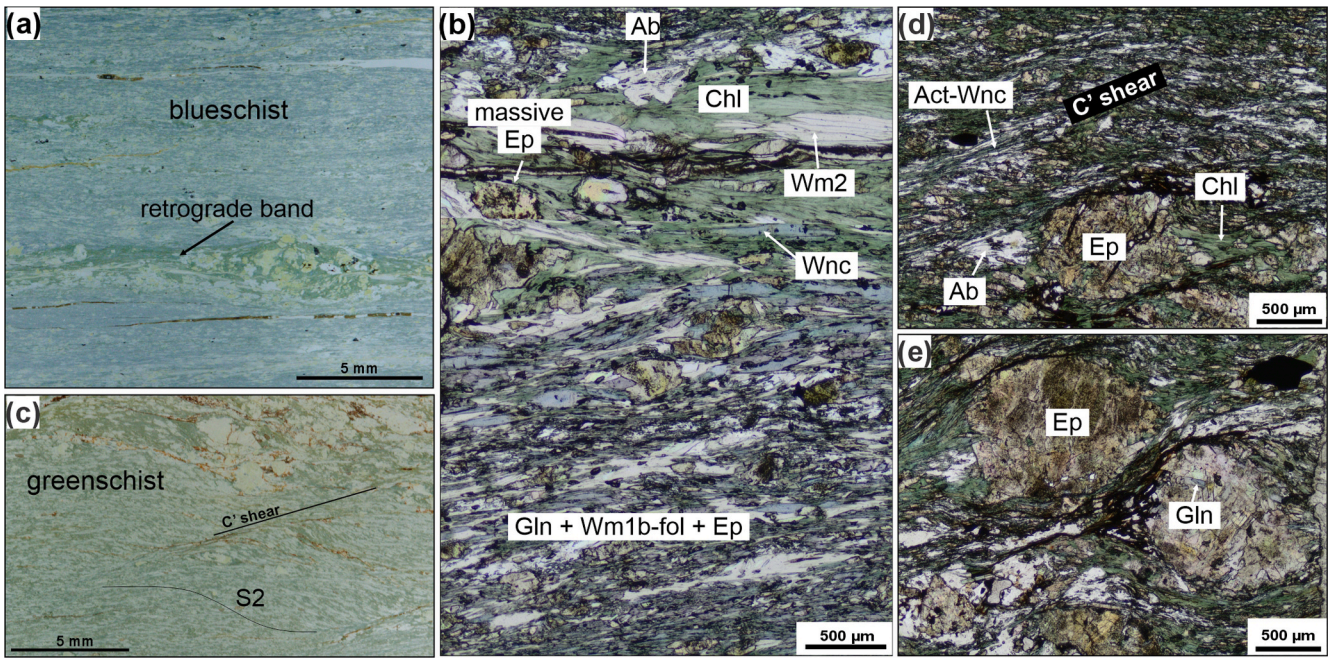

Fig. 7. Representative microscopic textures of the San Carlos-Manquemapu MA-18-77a locally retrogressed blueschist (a-b) and MA-18–67 strongly retrogressed blueschist transformed in greenschist (c-e). **(a)** Retrograde band. **(b)** Contact between blueschist zone made of glaucophane + WM1 white micas + elongated epidote and retroband of chlorite + massive epidote + albite + large WM2 white micas. **(c)** Main green S2 foliation with C' shear bands. **(d)** Epidote blasts with pressure shadows of chlorite and albite and C' shear bands made of actinolite, winchite and albite. **(e)** Glaucophane preserved in epidote blast. (For interpretation of the references to colour in this figure legend, the reader is referred to the web version of this article.)

(2016) are in agreement, displaying an average of 0.93 GPa for both WM1 and WM2.

4.2.1.2. Sector of San Carlos-Manquemapu. For the metamorphic peak of the MA-18-72 garnet-bearing blueschist, pressure estimates have been obtained with the Si-in-phengite barometers of Massonne and Schreyer (1987) and Kamzolkin et al. (2016). Detailed results are shown in Appendix 7. For the Massonne and Schreyer (1987) barometer, WM1a and WM1b give very similar pressure ranges of 0.96–1.08 GPa and 0.97–1.19 GPa, respectively. However, the barometric results obtained with the group 2 calibration of Kamzolkin et al. (2016) display higher pressures of 1.62–1.73 GPa for WM1a and 1.64–1.85 GPa for WM1b for 450 °C, in agreement with the results of our phase diagram from the next section.

For the retrograde event in MA-18-77 and MA-18-67, calculations were made for WM2 with the same Si-in-phengite barometers with a lower temperature of 350 °C, giving averages of 0.99 and 1.43 GPa for the first and second calibrations, respectively (Appendix 7). Chlorite in the three samples (MA-18-72 garnet-bearing blueschist, MA-18-77 retrogressed blueschist and MA-18-67 strongly retrogressed blueschist) texturally corresponds to the retrograde event. Thermometric results using calibrations of Cathelineau (1988) and Lanari et al. (2014) give averages of 312–289 °C and 375–312 °C, respectively (Appendix 7).

4.2.2. Phase equilibrium modeling

4.2.2.1. Sector of Guzmán. For the metamorphic peak of the retrogressed garnet-bearing amphibolite, we tried various phase diagrams with distinct reactive bulk chemical compositions calculated for GP-15-2C (Appendix 6). However, none of these tests gave consistent results regarding to the garnet isopleths and modal proportions of phases. The main problem is probably the presence of plagioclase along with epidote in the peak assemblage, for which relative proportions and composition are unknown. Also, the equilibrium volume of the peak conditions could have been modified by retrograde metamorphism in an open system, preventing correct calculations for the metamorphic peak.

For the retrograde event of the retrogressed garnet-bearing amphibolite, we constructed one phase diagram for the sample GP-15-2C, calculating the reactive bulk chemical composition using XMapTools and the micro-mapping method of Lanari and Engi (2017) (see Appendix 6) and selecting only the retrograde phases. We considered the following retrograde assemblage: actinolite + garnet rims + chlorite + epidote + titanite. In the resulting phase diagram (Fig. 8a), a stable field is delimited for the retrograde event at the intersection between the four end-member garnet rims isopleths (X_{Sps}: 0.18–0.23, X_{Prp}: 0.02, X_{Alm}: 0.38–0.43, X_{Grs}: 0.34—0.38; compositions of the rims extracted from XMapTools micro-mapping) and the aluminum content in actinolite (Al: 0.53–0.77). This stable trivariant field corresponds to the mineral association of Ep + Grt + Bt + Amp + Chl + Ttn + Ab + Qz under *P–T* conditions between 450 to 525 °C and 0.8 to 1.1 GPa. It should be noted that although the restricted area presents plagioclase and quartz, their modal proportions are negligible (~ 1 vol%).

4.2.2.2. Sector of San Carlos-Manquemapu. For the metamorphic peak of the MA-18-72 garnet-bearing blueschist, in order to determine the reactive bulk composition, we used the compositional map and subtract the volume of phases that grew during the prograde path (e.g. Grt1, Ca-rich glaucophane cores and Fe-rich epidote cores) to take into account fractionation. We also use various XFe^{3+} contents ($nFe^{3+}/(nFe^{3+}+nFe^{2+})$) and check the intersection fit of the Grt isopleths corresponding to the ultimate Grt1 rim to crystallize (X_{Sps}: 0.20–0.22, X_{Prp}: 0.027–0.033, X_{Alm}: 0.53–0.56, X_{Grs}: 0.21–0.24) and the Grt2 first increment (X_{Sps}: 0.24–0.28, X_{Prp}: 0.014–0.028, X_{Alm}: 0.45–0.50, X_{Grs}: 0.22–0.28). The best solution has been encountered for Grt2 first increment and $XFe^{3+} = 0.2$, which is a typical value for subducted mafic rocks (Massonne and Willner, 2008). The resulting phase diagram is shown in Fig. 8b. The tetravariant field defined by Amp + Chl + Ep + Grt + WM + Ttn + Qz + Rt, with *P–T* conditions between 425 and 475 °C and 1.5 and 1.7 GPa, corresponds well to the mineral association and phase volume modal proportions of the metamorphic peak. Few rutile is present (< 1.2 vol%), which would be in agreement with some

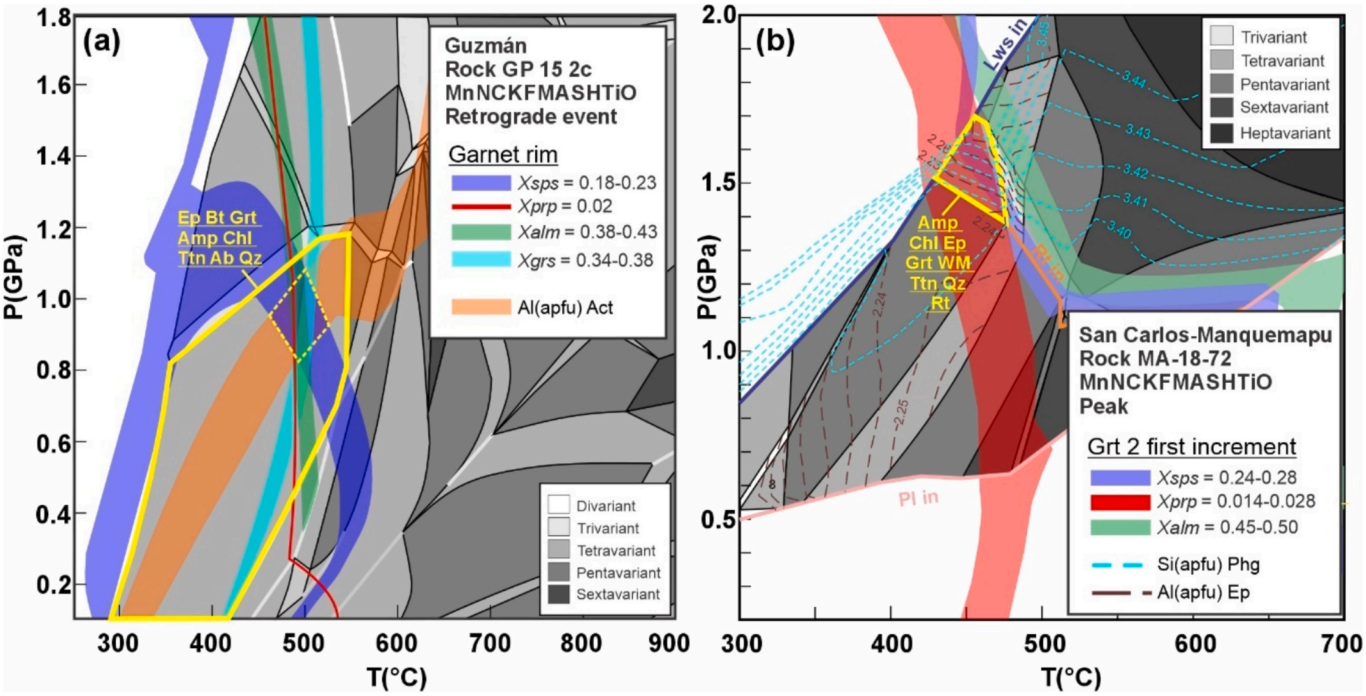

Fig. 8. Simplified phase diagrams calculated for **(a)** the retrograde event in the Guzmán GP-15-2C sample (retrogressed garnet-bearing amphibolite) and **(b)** the peak in the San Carlos-Manquemapu MA-18-72 sample (garnet-bearing blueschist). Full versions of the phase diagrams are provided in Appendix 7. Reactive bulk compositions used for the phase diagrams calculation were extracted using XMapTools micro-mapping (Lanari and Engi, 2017). **(a)** The *P–T* conditions estimated for the retrograde event of the Guzmán garnet-bearing amphibolite (dashed yellow diamond) are obtained through the mineral assemblage, intersection of compositional isopleths of the garnet rim and Al content in actinolite. **(b)** The *P–T* conditions estimated for the peak event of the San Carlos-Manquemapu garnet-bearing blueschist (bold yellow diamond) are obtained through the mineral assemblage, intersection of compositional isopleths of garnet and Si contents in phengite. (For interpretation of the references to colour in this figure legend, the reader is referred to the web version of this article.)

rutile observed within titanite. Si isopleths of phengite (WM1a and WM1b – Si_{apfu}: 3.40–3.46) also match this field.

4.3. Bulk rock geochemistry

The 40 analyzed rocks (Appendix 4) display L.O.I. between 1.28 and 4.89 wt% (except 2 samples with 7.27 and 10.85 wt%), in agreement with the occurrence of metamorphic hydrated minerals. Among the major elements, TiO_2 and P_2O_5 are generally considered immobile during metamorphism, and combined with REE and HFSE, are good magmatic petrogenetic indicators (Dilek and Furnes, 2011). Recalculated on an anhydrous basis, the bulk compositions show SiO_2 contents between 39 and 55 wt% (except the highly hydrated sample with only 32 wt% (chloritite) confirming elements mobilization), TiO_2 between 0.6 and 2.7 wt% (except the same sample with 3.3 %), Mg# (Mg/(Mg + Fe_{tot})) between 0.26 and 0.69, and K_2O contents higher in some blueschists (up to 5.3 wt%) and greenschist (2.3 wt%) in agreement with the presence of white micas. In the Zr/Ti *versus* Nb/Y diagram, the samples define four main clusters within the basalt and basaltic andesite fields (dashed ellipses in Fig. 9a). The first cluster lies near the N-MORB

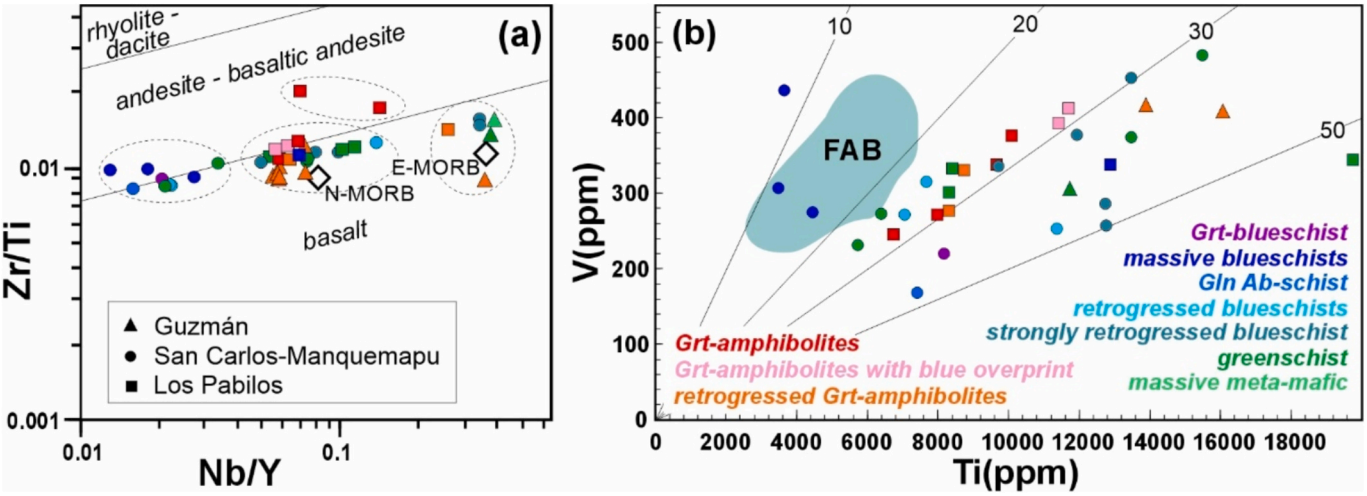

Fig. 9. **(a)** Zr/Ti – Nb/Y discrimination diagram after Winchester and Floyd (1977). **(b)** Ti-V diagram of Shervais (1982). Typical Ti/V ratios are from Dilek and Furnes (2011): 10–20 for island arc, 20–50 for MORB, 1–50 for back-arc basins. Field of fore-arc basalts (FAB) from Reagan et al. (2010). Symbol colors refer to lithotypes and symbol forms to localities. (For interpretation of the references to colour in this figure legend, the reader is referred to the web version of this article.)

composition and consists of Grt-bearing amphibolites with and without blueschist overprint (from Los Pabilos), retrogressed Grt-bearing amphibolites (from Los Pabilos and Guzmán), blueschist (from Los Pabilos), retrogressed and strongly retrogressed blueschists (from San Carlos-Manquemapu), and greenschists (from Los Pabilos and San Carlos-Manquemapu). The second cluster is close to the E-MORB composition and consists of retrogressed Grt-bearing amphibolites (from Los Pabilos and Guzmán), strongly retrogressed blueschists (from San Carlos-

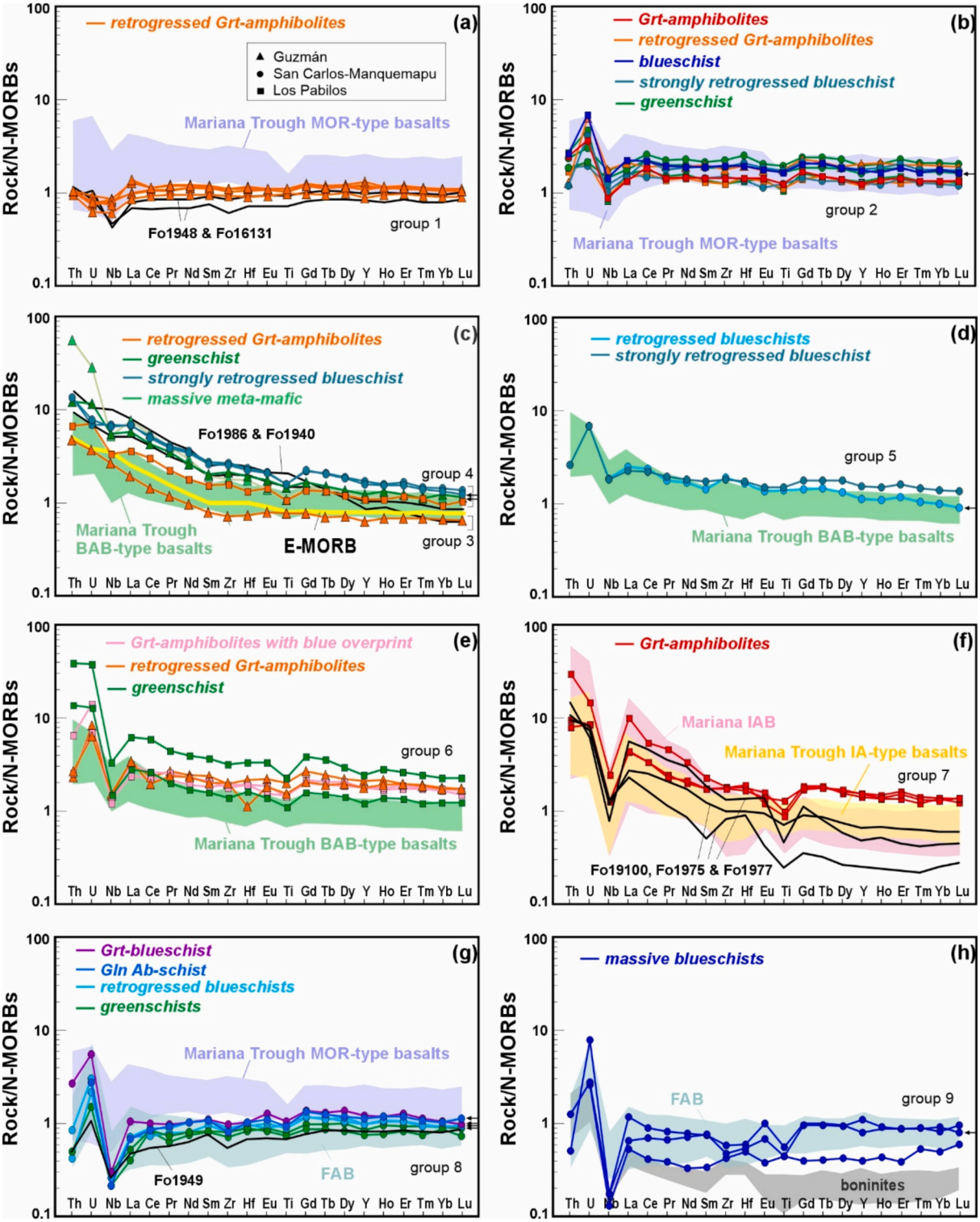

Fig. 10. N-MORBs-normalized spider diagrams. Normalization to N-MORB values of Sun and McDonough (1989). Fields of Mariana Trough rocks from Pearce et al. (2005): MOR-type (MORB with some possible subduction component signatures), BAB-type (a transitional type between MORB and IAB, with significant subduction component signatures) and IA-type (comparable to IAB). Field of Mariana IAB also from Pearce et al. (2005). Fore-arc basalts (FAB) and boninites are from Reagan et al. (2010). Black patterns "Fo" from Rapela et al. (2021) from mafic rocks associated to the Chaitenia back-arc. Same symbols as Fig. 9. Black arrows to the right of the patterns indicate samples with K_2O contents superior to 1.0 wt%. (For interpretation of the references to colour in this figure legend, the reader is referred to the web version of this article.)

Manquemapu), greenschist and massive meta-mafic rock (from Guzmán). The third cluster is lower in Nb and formed only from rocks of the San Carlos-Manquemapu area (blueschists, retrogressed blueschists and greenschists). Finally, the fourth cluster consists in two Grt-bearing amphibolites from Los Pabilos that depart towards the andesitic field. In the Ti/V diagram of Shervais (1982) (Fig. 9b), the majority of samples plots between Ti/V ratios of 20 and 50, similar to MORBs and back-arc basalts, whereas three blueschists display lower values similar to fore-arc basalts of Reagan et al. (2010).

Based on N-MORB-normalized multi-elements diagrams, nine main groups can be distinguished (Fig. 10). Group 1 consists of the retrogressed garnet-bearing amphibolites from Guzmán, showing flat patterns with trace element concentrations similar to N-MORBs, but with small Nb negative anomalies ($(La/Nb)_N$ of 1.1–1.9) (Fig. 10a). Group 2 is composed of various lithotypes coming from the three studied sectors (fresh and retrogressed Grt-bearing amphibolites, blueschist, strongly retrogressed blueschists, greenschists). They display flat patterns slighty more enriched than N-MORBs, except for Nb-negative anomalies ($(La/Nb)_N$ of 1.2–1.9), minor Ti-negative anomalies and U-positive anomalies (Fig. 10b). These two groups display patterns similar to those of MORBs from the Mariana back-arc basin (BAB) (Pearce et al., 2005). Group 3 is made of only one sample, a retrogressed Grt-bearing amphibolite from Guzmán, displaying a pattern comparable to E-MORB, with $(Nd/Yb)_N$ of 1.5 and without Nb anomaly ($(La/Nb)_N$ of 0.7) (Fig. 10c). Group 4, made of retrogressed Grt-bearing amphibolite of Los Pabilos, greenschist and massive meta-mafic rocks of Guzmán, and strongly retrogressed blueschists of San Carlos-Manquemapu, displays an enriched multi-element pattern that could resemble E-MORB, but with higher trace element concentrations and small Nb negative anomaly ($(La/Nb)_N$ of 1.0–1.5) (Fig. 10c). The latter is atypical for E-MORB and more akin to BAB or IAB. Group 5 consists of one retrogressed and one strongly retrogressed blueschists from San Carlos-Manquemapu. They display a slightly enriched pattern ($(Nd/Yb)_N$ of 1.3–1.7) and low Nb-negative anomalies ($(La/Nb)_N$ of 1.2–1.3) (Fig. 10d). Group 6, made of Grt-bearing amphibolites with blueschist overprint and greenschists from Los Pabilos, and retrogressed Grt-bearing amphibolite from Guzmán, is comparable to the precedent but displays marked Nb-negative anomalies ($(La/Nb)_N$ of 1.8–2.7) (Fig. 10e). Groups 5 and 6 are similar to BABs from the Mariana back-arc basin (Pearce et al., 2005). Group 7, made of Grt-bearing amphibolites from Los Pabilos, shows a LREE-enriched pattern

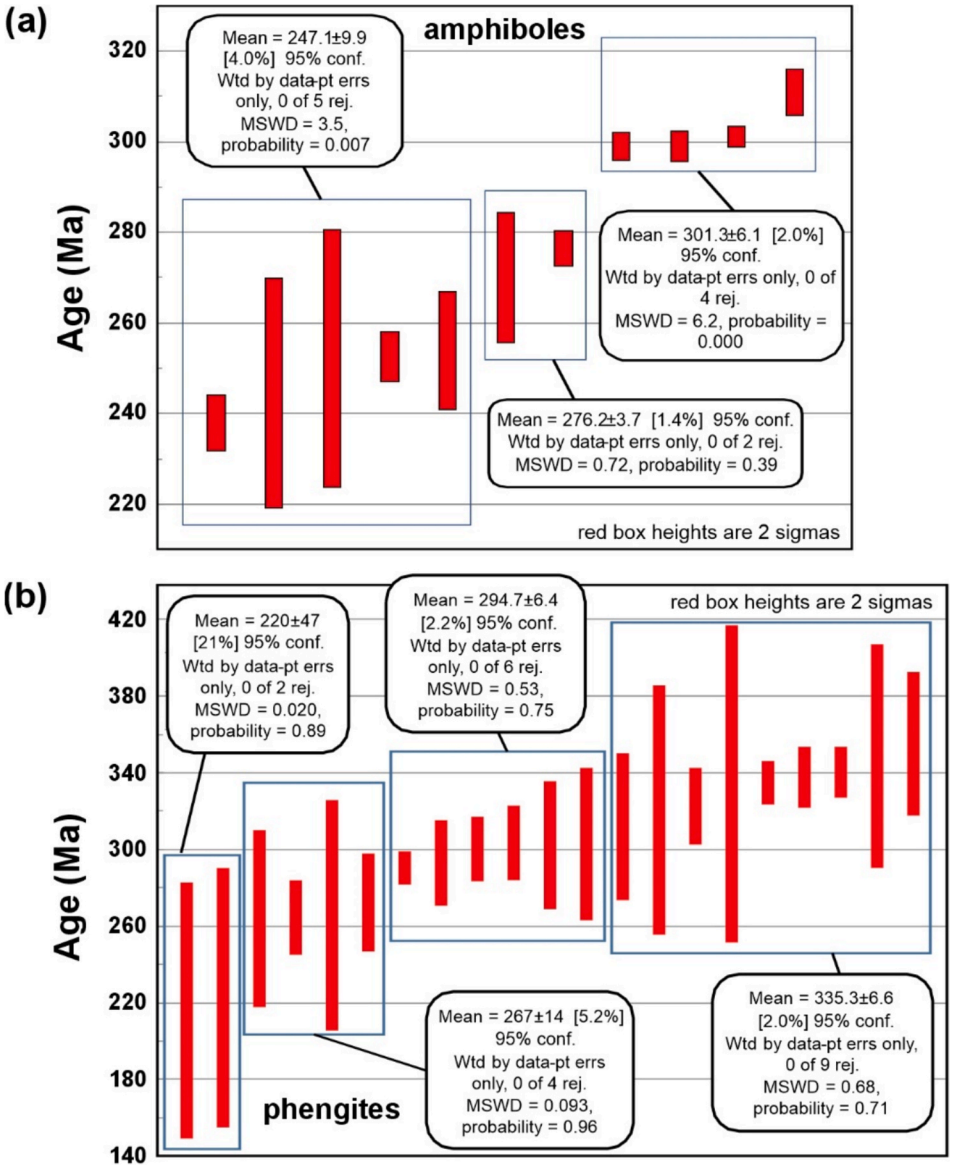

Fig. 11. **(a)** Amphibole *in situ* $^{40}Ar/^{39}Ar$ results for the Guzmán retrogressed garnet-bearing amphibolite GP-15-2C. **(b)** Phengite *in situ* $^{40}Ar/^{39}Ar$ results for the San Carlos-Manquemapu garnet-bearing blueschist MA-18-72.

((La/Sm)$_N$ of 2.5–4.4) with pronounced Nb-negative anomalies ((La/Nb)$_N$ of 3.4–4.1) and Ti-negative anomalies, comparable to island-arc type basalts from Mariana back-arc basin (Pearce et al., 2005) (Fig. 10f). Group 8, composed of Grt-bearing blueschist, retrogressed and strongly retrogressed blueschists, and greenschist from San Carlos-Manquemapu, displays a pattern similar to N-MORBs or slightly more depleted in trace elements and with a pronounced Nb-negative anomaly ((La/Nb)$_N$ of 1.7–3.5) (Fig. 10g). This pattern is similar to FABs from the Mariana fore-arc (Reagan et al., 2010). Finally, group 9, made of blueschists from San Carlos-Manquemapu, is depleted respect to N-MORBs, with the lowest Ti contents (0.58–0.74 TiO_2 wt%), and displays a LREE upwards-concave pattern and a pronounced Nb-negative anomaly ((La/Nb)$_N$ of 3.7–6.8) (Fig. 10h). This group is similar to FAB from the Mariana fore-arc (Reagan et al., 2010).

4.4. $^{40}Ar/^{39}Ar$ *in situ* dating

$^{40}Ar/^{39}Ar$ *in situ* dating of amphibole grains from the Guzmán retrogressed garnet-bearing amphibolite GP-15-2C (Fig. 11) yields minimum and maximum dates of 238.2 ± 6.2 and 311.2 ± 5.1 Ma (Appendix 5, errors are 2σ). It is possible to distinguish three date populations based on the means values: an older one with a range of 311.2 ± 5.1 to 299.2 ± 3.1 Ma; an intermediate one with two dates of 276.7 ± 4.0 and 270.3 ± 14.4 Ma, and a younger one with a range between 254.3 ± 12.9 and 238.2 ± 6.2 Ma. The older population is preserved in one large grain, whereas the intermediate and younger ones are preserved in various grains and generally at the rims (Appendix 5).

$^{40}Ar/^{39}Ar$ *in situ* dating of phengite grains from the San Carlos-Manquemapu garnet-bearing blueschist MA-18-72 (Fig. 11) yields minimum and maximum dates of 216.5 ± 33.0 and 355.1 ± 18.6 Ma (Appendix 5, errors are 2σ). Although they overlap when considering 2

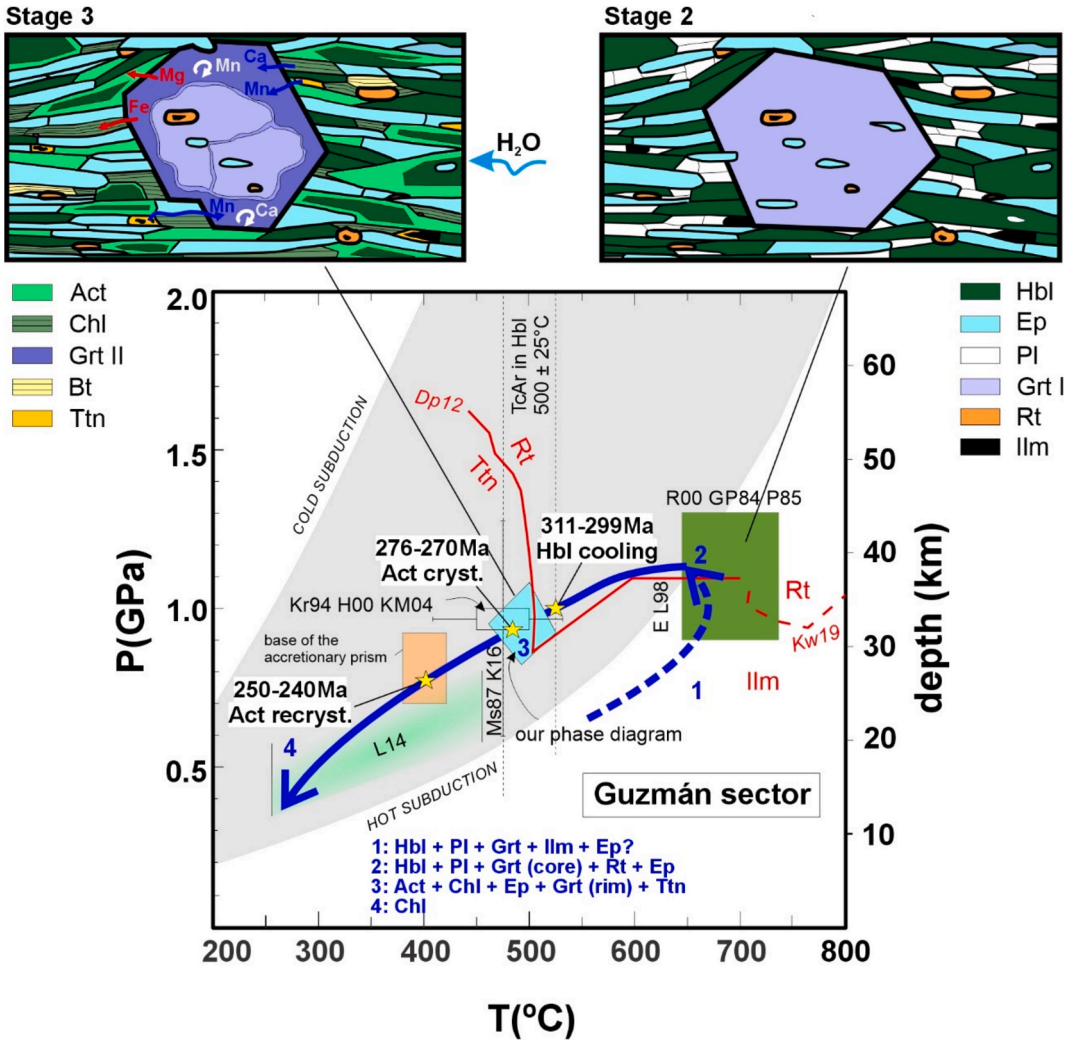

Fig. 12. *P–T–t* path interpreted based on the Guzmán GP-15-2C retrogressed garnet-bearing amphibolite and the GP-15-3 greenschist. The retrogressed garnet-bearing amphibolite recorded the metamorphic peak (Stage 2) and probably the high-*T* prograde path (Stage 1), as well as the retrograde path (Stages 3 and 4), while the greenschist recorded the metamorphic peak only in the hornblende cores and the Stages 3 and 4 in the majority of the rock. Stage 1 (prograde path in segmented lines) defined in GP-15-2C, inferred from incomplete consumption of ilmenite surrounded by rutile seen in garnet inclusions. Box of Stage 2 (near-metamorphic peak) obtained from geothermobarometry on peak mineral assemblage (thermometers: R00 Ravna, 2000; GP84 Graham and Powell, 1984; P85 Perchuk et al., 1985; barometer: EL98: Ernst and Liu, 1998). Stage 3 defined by our phase diagram from retrograde mineral assemblages from GP-15-2C and by geothermobarometry (Bt-Grt rim thermometers KR94 Kleeman and Reihnardt 1994; *H*00 Holdaway, 2000; KM04 Kaneko and Miyano, 2004; barometer Si in phengite K16 Kamzolkin et al., 2016). Stage 4 defined only for temperatures (pressures being not constrained) based on chlorite thermometry L14 (Lanari et al., 2014). Red stability limits of rutile in metabasites from Diener and Powell (2012) (Dp12) and Kunz and White (2019) (Kw19). Worldwide *P–T* estimates subduction records as grey field from Penniston-Dorland et al. (2015). *P–T* for the box of the base of the accretionary prism from Glodny et al. (2005) and Willner (2005). (For interpretation of the references to colour in this figure legend, the reader is referred to the web version of this article.)

sigma errors, it is possible to distinguish four date populations based on the means values: an older one with a mean of 335.3 ± 6.6 Ma, a second one with a mean of 294.7 ± 6.4 Ma, a third one with a mean of 267 ± 14 Ma and a younger one with two dates averaging at 220 ± 47 Ma. Texturally, the older population is preserved in the S1a microlithons but also in the S1b cleavage zones (Appendix 5). The second population is observed in the S1b cleavage and in the epidote-white mica boudin. The third and fourth populations are randomly distributed inside S1a microlithons and S1b cleavage zones.

5. Discussion

5.1. P–T–t paths and regional correlations

5.1.1. Guzmán sector

The prograde path in the Guzmán amphibolites is recorded in the occurrence of ilmenite surrounded by rutile, both phases included in garnet core (Fig. 3d). For mafic protoliths, experimental studies on MORB composition have shown that rutile is stable at pressures above 1.2 GPa while ilmenite would be stable at high temperatures (~750 °C at 1.2 GPa) and titanite corresponds to the lower temperature and lower pressure phase (Liou et al., 1998). Similar stability fields distribution has been obtained in phase diagrams for metabasic rocks, although their limits depend on the bulk rock composition and the solution models used (Diener and Powell, 2012; Kunz and White, 2019). The fact that ilmenite is surrounded by rutile could correspond to its incomplete consumption when the rock was subjected to higher pressures and probably higher temperatures (Stage 1, Fig. 12a). We thus consider that the rock first passed into the amphibolite facies at pressures below 1.0 GPa (Stage 1), when the probable paragenesis was Hbl + Grt + Pl + Ilm ± Ep.

It further reached its metamorphic peak between 645 and 735 °C as suggested by conventional Grt-Hbl core thermometry (Appendix 7). The peak assemblage was formed of Hbl + Grt (core) + Rt ± Ep (+ Pl?) (Fig. 12a, Stage 2). The high temperature estimations are in agreement with the homogenous chemical profiles of garnet cores, suggesting that diffusion took place when the rock was heated during a relatively long period at temperatures ≥ 700 °C (Ayres and Vance, 1997). However, as no evidence of partial melting has been found, the peak likely occurred in the lower range of these temperature estimations (i.e. ~ 650 °C, Fig. 12a, Stage 2). For the pressure estimates, the empirical barometer of Ernst and Liu (1998) based on Al_2O_3 in calcic amphiboles gives values from 1.0 to 1.2 GPa considering the temperatures obtained in the garnet core, which is consistent with the pressures estimated for rutile stability in metabasites (Diener and Powell, 2012; Kunz and White, 2019). Thus, the *P–T* estimates overall point to a hot subduction path (Penniston-Dorland et al., 2015) (Fig. 12a). Such conditions were already recognized in other sectors of the Western Series. In Punta Sirena (~34°S), it is recorded in garnet-bearing micaschists and amphibolites with peak *P–T* conditions of 1.25–1.4 GPa/ 540–580 °C and 0.95–1.0 GPa/ 540–575 °C respectively, at ca. 336–330 Ma (Hyppolito et al., 2014b). In the Los Pabilos sector (~41°S), the boulders of garnet-bearing amphibolites and *retro*-eclogites recorded peak conditions of 1.0–1.4 GPa/500–550 °C at 361 Ma ($^{40}Ar/^{39}Ar$ in hornblende; Kato et al., 2008). These amphibolite facies *P–T* conditions and reconstructed counterclockwise trajectories have been linked to the onset of a subduction system, characterized by a warm hanging mantle (e.g. Peacock, 1987; Willner, 2005; Hyppolito et al., 2014b). In the La Cabaña ultramafic rocks adjacent to the Guzmán amphibolites from this study (Fig. 2a), metamorphic olivine-bearing mylonitic antigoritites recorded peak *P–T* conditions of 1.1 GPa and ~ 600 °C (Plissart et al., 2019). Thus, both rocks reached depths of ca. 35–45 km following a hot *P–T* path that we interpret as resulting from a still thermally immature subduction system (Fig. 12a).

Following peak metamorphism, the Guzmán amphibolites cooled down nearly isobarically to 500 °C (Fig. 12a, path between Stage 2 and Stage 3), defining thus a counterclockwise *P–T* trajectory. This path suggests an initial warm subduction gradient, gradually cooling. Our *in situ* amphibole $^{40}Ar/^{39}Ar$ oldest ages population (Fig. 11a) corresponds to the time when the rock cooled down to the closure temperature of hornblende, estimated at 500 ± 25 °C (Harrison, 1981). The 311–299 Ma ages thus correspond to the cooling path just before reaching Stage 3, while the peak conditions would be older. In comparison, in Punta Sirena, the rocks after the peak were incorporated at 308 Ma at the base of the accretionary prism ($^{40}Ar/^{39}Ar$ in phengites; Willner et al., 2005; Hyppolito et al., 2014b) and, in Los Pabilos, they underwent a retrograde blueschist overprint of 1.0–1.2 GPa/420–425 °C at 325 Ma (Willner et al., 2004; Kato et al., 2008).

Stage 3 is characterized by a significant hydration event at depths of 30–35 km (0.8–1.1 GPa) and temperatures of 480–520 °C, forming the paragenesis of Grt II + Act + Ep + Chl + Ttn ± Bt (Fig. 12a). These *P–T* conditions are different from the ones obtained for the base of the Chilean late Paleozoic mature accretionary prism (0.7–0.9 GPa and 380–420 °C; Glodny et al., 2005; Willner, 2005), reflecting slightly greater depths with the corresponding hotter isotherms. Thus, an important circulation of fluids occurred in the subduction channel, deeper than the base of the accretionary prism, possibly in its "tail". Our second amphibole $^{40}Ar/^{39}Ar$ age population (276.7 ± 4.0 and 270.3 ± 14.4 Ma; Fig. 11a) corresponds to the cooling of the hornblende rim and/or the crystallization of the actinolite during the hydration event. It is similar within error to nearby ages of 283.4 ± 7 Ma and 285.5 ± 7 Ma obtained on metasomatic zircons encountered in the blackwall and inside fractures of chromitites from the La Cabaña massif (Romero et al., 2017). It also matches the age of 282 ± 6 Ma obtained by K-Ar on fuchsite from host metasediments (Höfer et al., 2001) and interpreted as the age of Cr mobilization coming from the ultramafic rocks during their emplacement into the metapelites. All the above points to the fact that Stage 3 hydration event was recorded both in the Guzmán amphibolites and in the La Cabaña ultramafic rocks, thus implying that they were located close to metasediments and share a common evolution since that time.

Finally, following Stage 3, the meta-mafic rocks cooled down to temperatures of 450–250 °C, as documented in chlorites (Appendix 7). This cooling should be linked to the exhumation inside the prism (Stage 3 to 4, Fig. 12a). Along this path, the rocks first passed by the conditions estimated for the base of the mature accretionary prism (~420–380 °C and 0.7–0.93 GPa; Glodny et al., 2005; Willner, 2005). Our youngest amphibole $^{40}Ar/^{39}Ar$ ages (ca. 250–240 Ma, Fig. 11a) could have registered actinolite recrystallization under these conditions. The rocks further exhumed at shallower levels inside the prism, due to ongoing basal accretion and erosion (Glodny et al., 2005).

5.1.2. San Carlos-Manquemapu sector

The prograde path in the MA-18-72 garnet-bearing blueschist is preserved in the chemical zoning observed in glaucophane, garnet and epidote (Fig. 6). Glaucophane displays a Ca-rich core testifying for lower pressure conditions. Garnet core (Grt1) shows a typical prograde Mn decrease and Fe increase from core to rim (Fig. 6). Epidote is characterized by an enrichment in Al in its rim (Fig. 6), which corresponds to pressure increase according to the distribution of isopleths for our phase diagram (Fig. 8b). No evidence of phases crystallizing at higher temperatures have been found. We thus consider that the rock followed a cold subduction gradient, from greenschist to blueschist facies conditions (Stage 1, Fig. 13).

The metamorphic peak (Stage 2, Fig. 13) corresponds to the end of the prograde path and thus the ultimate rim of Grt1 to crystallize (Fig. 6). At this stage, glaucophane is Na-rich and epidote, according to the isopleths (Fig. 8b), crystallized with higher Al contents than during the prograde path. Together with white micas, they formed the S1a foliation. Rutile also crystallized at this stage. The *P–T* conditions registered by this stage would be the tetravariant field from our phase diagram (~ 1.6 GPa – 450°C). Compared to blueschists from other sectors of the Western Series, they preserved higher pressures

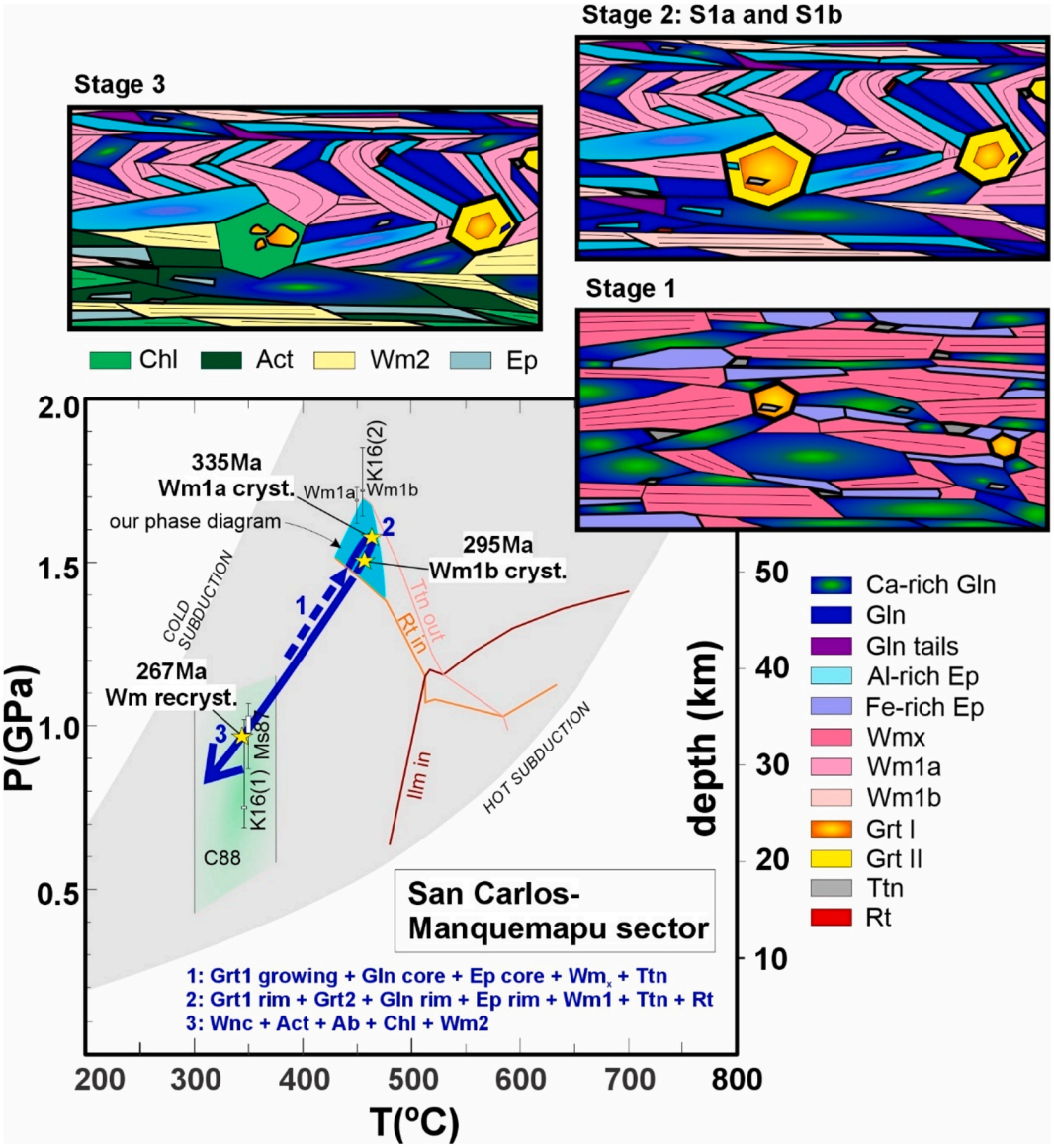

Fig. 13. *P–T–t* path interpreted based on the San Carlos-Manquemapu MA-18-72 garnet-bearing blueschist and MA-18-77 and MA-18-67 locally and strongly retrogressed blueschists. The blueschist and locally retrogressed blueschist recorded the metamorphic peak and the retrogression event at high-*P* (Stage 2), as well as the retrograde path (Stage 3) while the strongly retrogressed blueschist recorded nearly only the retrogradation (Stage 3). Stage 1 (prograde path in segmented lines) defined in MA-18-72, inferred from relict cores of Ca-Amph, zoning in Grt 1 and in Ep. Stage 2 (metamorphic peak and high-*P* retrogradation) obtained from mineral assemblage and Grt 2 and WM1 isopleths distribution. Stage 3 (low-*P* retrograde stage) obtained from geothermobarometry (barometer: K16 Kamzolkin et al. (2016); Ms87 Massonne and Schreyer (1987); thermometer: C88 Cathelineau (1988)). Stability field of Ti phases from our phase diagram. Worldwide *P–T* estimates subduction records as grey field from Penniston-Dorland et al. (2015).

(Pichilemu blueschists: 0.95–1.07 GPa and 380–420 °C (Willner, 2005; Halama and Konrad-Schmolke, 2015; Muñoz-Montecinos et al., 2020); Los Pabilos blueschist overprint on *retro*-eclogites: 1.0–1.2 GPa and 420–425 °C (Willner et al., 2004; Kato et al., 2008)), reaching depths of ~ 55 km for ~ 475 °C in the epidote-blueschist facies (Fig. 13). Moreover, the high-*P* retrograde path recorded by the growth of Grt2 in equilibrium with glaucophane, epidote and white mica 1 (Figs. 5, 6) probably occurred in the same tetravariant field and along a similar metamorphic gradient to the prograde path, defining a hairpin trajectory (Fig. 13). S1 white micas equilibrated during Stage 2 at least between 335 Ma (WM1a) and 295 Ma (WM1b), as shown by our *in situ* $^{40}Ar/^{39}Ar$ results (Fig. 11). Indeed, as the closure temperature for white micas is estimated at 425 °C at 1.0 GPa and possibly as high as 550 °C under blueschist conditions (Harrison et al., 2009), our phengite $^{40}Ar/^{39}Ar$ ages correspond to (re)crystallization ages, with preservation of two events (S1a and S1b). We suggest that S1a corresponds to the metamorphic peak and that S1b, associated with a simple shear event (Fig. 5), formed during the high-*P* exhumation (near-peak). Our ages are in good agreement with previous results obtained by Kato et al. (2008) for the retrogradation of the Los Pabilos amphibolite under blueschist facies conditions (325 Ma $^{40}Ar/^{39}Ar$ in white micas). Thus, regarding the evolution of the subduction system in this sector, its inception would have begun prior to 361 Ma, as showed by $^{40}Ar/^{39}Ar$ results on hornblende from a garnet-bearing amphibolite from Los Pabilos (Kato et al., 2008) and was probably almost steady-state at 340 Ma.

After the high-*P* exhumation, the rocks reached the return flow zone of the subduction channel and exhumed up to the base of the accretionary prism, defining a low-*P* retrograde path (Stage 3, Fig. 13) characterized by winchite, actinolite, epidote, chlorite and albite (Figs. 5-7) with temperature estimates of 300-375 °C. The third population of our $^{40}Ar/^{39}Ar$ white mica ages (267 Ma) could correspond to the moment when the mafic rocks stayed at the base of the prism where

they re-equilibrated under greenschist conditions and white micas recrystallized. Finally, the two recrystallized ages of ~ 220 Ma would correspond to conditions inside the accretionary prism.

5.2. Tectonic setting of formation of the mafic protoliths

The rocks of this study can be divided into eight groups related to a subduction environment if compared with the well-documented back-arc basin (BAB) of the Mariana system (Figs. 10, 14), comprising N-MORBS with weak subduction signals, BABBs, IABs and FABs (Pearce et al., 2005, Reagan et al., 2010), except for one retrogressed amphibolite (group 3) that displays a pattern similar to E-MORB. On the Ti-Mn-P plot, the rocks plot mainly between the fields of MORBs, island arc tholeiites and island arc calc-alkaline basalts, with three of them in the OIB field (Fig. 14a). Similar results are obtained in the Y-La-Nb diagram, but with one sample plotting in the E-MORB composition and four samples in the continental basalt field (Fig. 14b). These correspond to our group 3 and 4 of Fig. 10. In the Th/Yb-Nb/Yb diagram (Fig. 14c), one group of samples plot along the MORB-OIB array, which would indicate very small subduction contaminant in the mantle source, whereas others are enriched in Th and plot above the array, in agreement with the imprint of slab-derived components in the source. Additionally, various samples in the MORB-OIB array are more depleted than N-MORB, corresponding to the fore-arc basalts alike-groups. Two samples plot near the E-MORB composition. Finally, in the back-arc discrimination diagram of Hollocher et al. (2012) (Fig. 14d), one group is very similar to the field of mature back-arc basins with little subduction components (like the older part of the Lau Basin) whereas the second distributes in the BABs field towards the compositions of continental arc lavas. Note that there are no positive correlations between the K_2O contents and the Nb negative anomaly nor the LREE enrichment (see Fig. 10 for details). We thus conclude that the patterns really reflect the tectonic setting of the protoliths.

All together, these comparisons suggest that the Guzmán, Los Pabilos and San Carlos-Manquemapu mafic protoliths originated in a back-arc basin and oceanic arc system. Geochemical variations are likely due to

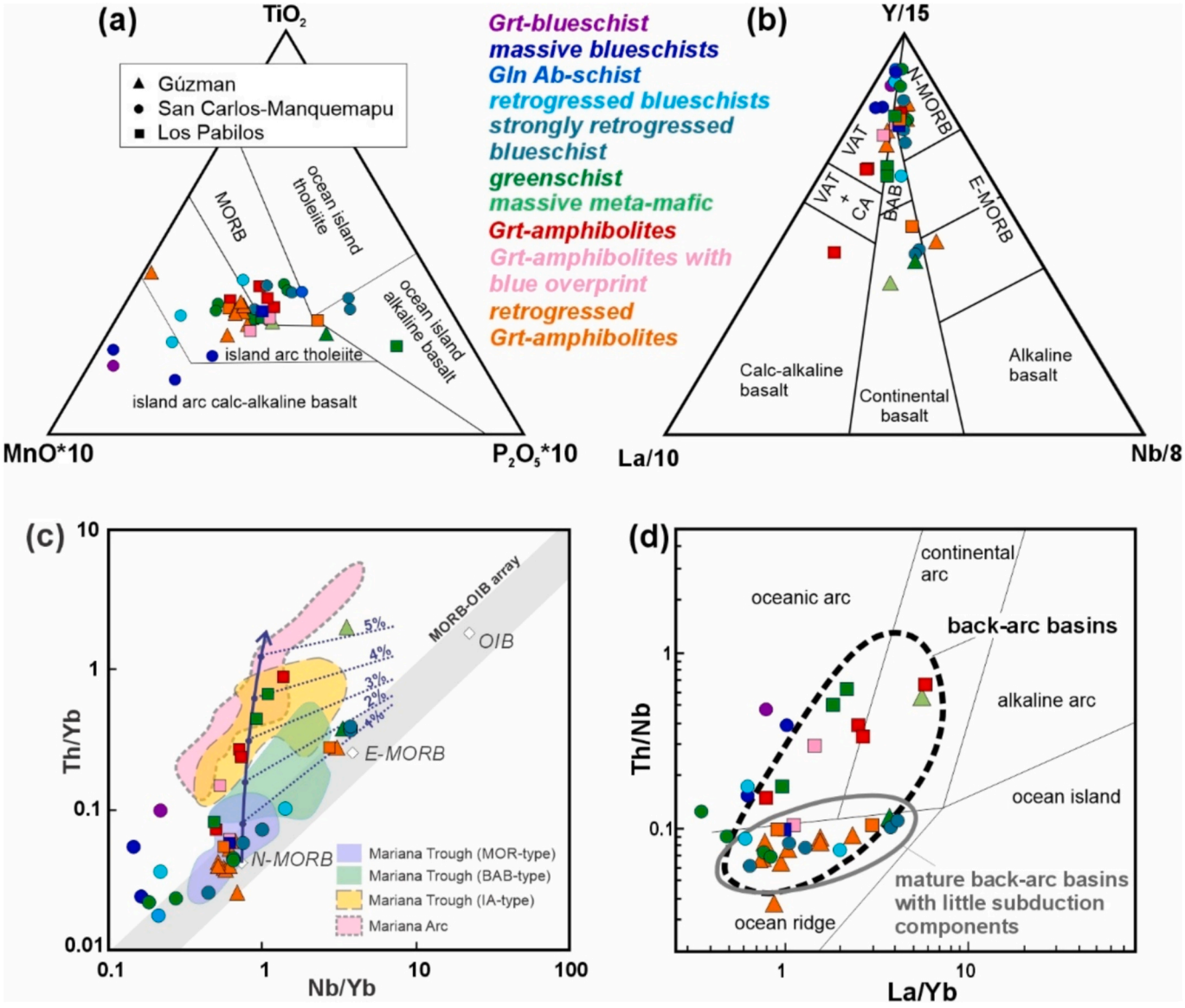

Fig. 14. Discriminant diagrams for tectonic settings of the studied mafic rocks. **(a)** Ti-Mn-P diagram of Mullen (1983). **(b)** Y-La-Nb diagram of Cabbanis and Lecolle (1989). **(c)** Th/Yb – Nb/Yb diagram and percentages of subduction contamination of Pearce (2008). Fields of Mariana Trough (MOR-, BAB-, IA-types) and Mariana Arc basalts from Pearce et al. (2005). **(d)** Th/Nb-La/Yb back-arc basin discriminant diagram of Hollocher et al. (2012). Same symbols for the four diagrams. (For interpretation of the references to colour in this figure legend, the reader is referred to the web version of this article.)

"subduction sampling" of different parts of this system. At the beginning of a back-arc basin extension, the spreading center is located near the trench and thus the mantle source experiences important slab-derived metasomatism. Later, in a large mature back-arc where the spreading center is located much further away from the trench, the mantle would show almost no influence from the slab (Pearce et al., 2005). The same basin thus shows spatial and temporal geochemical variations, characterized by older arc-like rocks in its borders and younger MORB-like rocks in its center. Finally, the samples plotting in the E-MORB and continental basalt fields could correspond to low degrees of partial melting as suggested by Rapela et al. (2021) or to local variations of the mantle source inside the back-arc system. Indeed, basalts with similar E-MORBs patterns are encountered in modern back-arcs (e.g. Izu-Bonin-Mariana: Metcalf and Shervais, 2008; East Scotia: Pearce and Stern, 2006), where they record melting of an enriched mantle component mobilized during rifting (Pearce and Stern, 2006). Alternatively, the E-MORBs could have originated in another setting, like the wide ocean subducted beneath the SW Gondwanan margin at the end of the Paleozoic in which such signature is common (Hyppolito et al., 2014a). In that case, their accretion in the prism and juxtaposition with the metasediments and mafic rocks issued from the back-arc would be fortuitous.

The above interpretation of a back-arc basin setting agrees with the presence of chromitites inside the ultramafic massif of La Cabaña near Guzmán (Fig. 2a), which display Cr# in chromite cores higher than 0.65, typical of suprasubduction zone settings (González-Jiménez et al., 2014). Those authors already suggested that the chromitites crystallized in dunite channels beneath a spreading center that opened as a marginal basin above a supra-subduction zone (González-Jiménez et al., 2014). Also, the high Fo contents of mantle olivine from the massive partially serpentinized peridotites and schistose serpentinites of La Cabaña are consistent with high rates of hydrous partial melting typical of the suprasubduction mantle (Plissart et al., 2019). We thus interpret that the mafic and ultramafic rocks from the Guzmán-La Cabaña sector originated in the same back-arc setting (see also Donoso-Tapia et al., 2024). Further, when comparing our chemical results with the mafic rocks of Rapela et al. (2021) from the Pacific Devonian Domain of NW Patagonia, they distribute in our groups 1, 4, 7 and 8 (Fig. 10). Those authors also interpreted their rocks as formed in a marginal basin, more specifically the Chaitenia back-arc basin.

5.3. Tectonic implications for the late Paleozoic SW Gondwanan margin at present latitudes of Central and South Chile

5.3.1. Current interpretations

After Ordovician times, the SW Gondwanan margin would have been affected by the accretion of three main tectonics blocks: the Chilenia, Chaitenia and Southern Patagonia blocks (Fig. 1), whose evolution and spatial limits are so far unclear. It is interpreted that these three blocks accreted to an already multi-composed Gondwanan margin made of Cuyania and the North Patagonian massif. Indeed, based on detrital zircons population, the Cuyania terrane would have rifted from southern Laurentia (Ouachita embayment) and further collided with SW Gondwana during the Middle Ordovician, as shown by syncollisional magmatism and regional metamorphism ages (Thomas and Astini, 2003; Ramos, 2009). With respect to the North Patagonian massif, the continuity of Famatinian and Pampean magmatic belts in its northern part suggests that it has been autochthonous or parautochthonous relative to Gondwana since the Siluro-Devonian (Pankhurst et al., 2006; Pankhurst et al., 2014) or possibly since Cambro-Ordovician times (Rapela and Pankhurst, 2020; Rapalini et al., 2013).

The Laurentia-derived Chilenia terrane would have collided on this multi-composed margin during Devonian times at ca. 390–385 Ma, as suggested by the age of the Guarguaráz metamorphic complex interpreted as formed during the collision (e.g. Willner et al., 2011; Hyppolito et al., 2014a). However, the subduction polarity is still debated, which will be discussed in detail in Section 5.3.3. The Chaitenia oceanic arc micro-block has been defined by Hervé et al. (2016) and Hervé et al. (2018) based on O and Hf isotopes on Devonian zircons from granitic intrusions and from metasediments of the southern Chile accretionary complex. This micro-block is thought to have drifted away from the North Patagonian fore-arc continental margin around 395–390 Ma based on U-Pb on zircons from the Zarao trachyte; Hervé et al., 2016; Hervé et al., 2018). The associated oceanic arc remained active from ~ 395 to 358 Ma (U-Pb on zircons from Pichicolo, Río Blanco and Lago Yelcho intrusions), implying the opening of the Chaitenia back-arc, as recognized by Rapela et al. (2021) from the geochemical signatures of mafic rocks. The reestablishment of a continental arc (Curruhué-Cáceres intrusions) at 380–365 Ma suggests that the Chaitenia back-arc would have rapidly closed and the Chaitenia oceanic arc collided with the same margin from which it originated at 360–340 Ma (Rapela et al., 2021). As for the Southern Patagonia, it would have collided later with the North Patagonian Massif, during mid-Carboniferous times, following an early-Carboniferous NE-directed subduction of the interposed oceanic basin (Pankhurst et al., 2006).

5.3.2. New latitudinal extension of the Chaitenia back-arc

Low $\delta^{18}O$ values in zircons from the Zarao trachyte, formed during the early stage of rifting, led Rapela et al. (2021) to propose that the Chaitenia oceanic arc and its associated back-arc extend northward to at least 41°19′S. The sectors of Los Pabilos and San Carlos-Manquemapu are located nearby, at ~ 40°57′S and ~ 40°54′S while the sector of Guzmán is located significantly farther north, at ~ 38°33′S. There, a Devonian detrital zircon age population of 365–380 Ma has been reported in the enclosing schists of the La Cabaña ultramafic body (Romero et al., 2017). These authors interpreted these ages as evidence of an island arc/back-arc system to the west of the continental margin, in a geometry very similar to the system proposed for Chaitenia. Our new geochemical results on meta-mafic rocks (Figs. 10, 14), combined with published evidence in the ultramafic La Cabaña massif already detailed in the section 5.2 (González-Jiménez et al., 2014; Plissart et al., 2019), also favor the presence of a back-arc at the current latitudes of 38°S. We thus consider that the Chaitenia arc and back-arc system extended north up to the Lanalhue Fault Zone (LFZ). In contrast, north of the LFZ, bulk chemical results from the meta-mafic rocks incorporated in the late Paleozoic Chilean accretionary prism (~ 34°S) display N-MORBs, E-MORBs and OIBs signatures, without evidence of oceanic arc-derived patterns, interpreted by Hyppolito et al. (2014a) as a heterogeneous subducted oceanic crust, characterized by seamounts on top of variously plume-enriched and temporarily distinct mid-oceanic crust (Muñoz-Montecinos et al., 2024) and absence of BAB environment.

In addition, this spatial distribution could be associated with the southern limit of Chilenia (Fig. 1). Interestingly, the Chaitenia oceanic arc micro-block would have drifted from the North Patagonian fore-arc continental margin at similar times (393 ± 3 Ma and 392 ± 2 Ma for Chaitenia intrusions; Hervé et al., 2016; Hervé et al., 2018; Rapela et al., 2021) than the Chilenia collision (390 ± 2 Ma for the metamorphic peak of the Guarguaráz complex; Willner et al., 2011) so that a spatial and temporal relationship could exist between both tectonic events. Here, we infer that a close relationship could exist between (i) the collision of Chilenia against the SW Gondwanan margin and (ii) the opening of the Chaitenia back-arc. As the subduction and collision polarities between Chilenia and Cuyania are significant for our hypothesis but are still debated, we review the current interpretations and models in the next section.

5.3.3. The Chilenia terrane and its collision

The existence of the Chilenia terrane was first proposed by Ramos et al. (1986), based on a belt of mafic and ultramafic rocks in the western Precordillera and eastern Frontal Cordillera (30–34°S), interpreted as remnants of an oceanic suture between Cuyania and a distinct terrane (Fig. 1). Exposures of basement units attributed to Chilenia are

uncommon and largely intruded or covered by Late Paleozoic intrusions, Choiyoi volcanics, and younger sedimentary sequences. Possible remnants include the Guarguaráz Complex (Fig. 1; Álvarez et al., 2011). A Laurentian origin is often inferred for Chilenia, based on Grenvillian-age zircons (Boedo et al., 2020). Two main models have been proposed: (i) Chilenia as an allochthonous terrane that rifted from Laurentia after Cuyania (e.g., Hyppolito et al., 2014a) or (ii) as part of a composite Cuyania–Chilenia block, separated by a narrow oceanic basin (e.g., Boedo et al., 2021). The oceanic basin between Cuyania and Chilenia likely opened during the late Neoproterozoic to Early Devonian, as suggested by fossil evidence, U–Pb zircon ages, and Nd model ages (Davis et al., 2000; Pérez Luján et al., 2021). Geochemical and isotopic data from mafic rocks in the suture show N-MORB and E-MORB affinities, interpreted as products of plume activity linked to the Iapetus Ocean opening and terrane rifting (Boedo et al., 2021; Pérez Luján et al., 2021). The closure of the basin is recorded by HP-LT metamorphism in mafic rocks from the Peñasco area (0.7–0.9 GPa, 345–395 °C; Boedo et al., 2021) and by higher-pressure conditions in the Guarguaráz Complex (1.2–1.4 GPa, 470–530 °C), followed by decompression with heating—typical of continent–continent collision (Massone and Cálderon, 2008; Willner et al., 2011). The collision, often attributed to the Chanic phase, has been dated to the Devonian (~390 Ma Lu–Hf in garnet; Willner et al., 2011). However, the polarity of subduction – whether east-dipping beneath Cuyania or west-dipping beneath Chilenia (in actual coordinates) – remains debated.

Two main lines of evidence have been used to resolve the subduction direction: the location of the Devonian continental arc associated with the subduction and the vergence of deformation associated with the collision. The main data in favor of a west-dipping subduction are (i) the presence of calc-alkaline intrusions at the west of the supposed suture, in the Frontal Cordillera (Papagayos, Carrolitza, Pampa de Las Avestruces; 413 ± 2 Ma to 389 ± 3 Ma; Dahlquist et al., 2020; Dahlquist et al., 2021) and (ii) top-to-the east structures in the W Precordillera interpreted as formed in the pro-wedge above a west-dipping subduction beneath Chilenia (Davis et al., 1999; Cingolani and Ramos, 2017; García-Sansegundo et al., 2023) whereas those in favor of an east-dipping subduction are (i) the presence of calc-alkaline intrusions at the east of the supposed suture, in the San Rafael block (Rodeo de la Bordalesa; 401 Ma; Cingolani and Ramos, 2017) and in the Agua Escondida region (La Menta and Borborán; c. 388 and 377 Ma; Cingolani and Ramos, 2017 and references therein), (ii) the presence of large batholiths and smaller bodies (405 ± 9 Ma and 359 ± 5 Ma) in the Sierras Pampeanas with I-type, A-type and adakitic signatures interpreted as resulting from eastwards directed flat-slab subduction during the Devonian, with delamination and melting far away from the trench (Dahlquist et al., 2021 and references therein) and (iii) top-to-the west structures developed in the Frontal Cordillera (Giambiagi et al., 2014; Boedo et al., 2021) and the Guarguaráz Complex (García-Sansegundo et al., 2016). From all the above, we conclude that the current data are still insufficient to determine the direction of subduction.

5.4. Geodynamic build-up of the late Paleozoic SW Gondwanan margin at present-day latitudes of central and South Chile

5.4.1. Possible motor for the Chaitenia back-arc opening

The most common mechanism proposed for BABs formation is slab rollback, driven by slab pull from negatively buoyant, old, and cold oceanic lithosphere, which promotes trench retreat (Artemieva, 2023). BABs formed in ocean–continent settings are typically short and rarely evolve into full seafloor spreading. Based on a review of actual and extinct BABs, Artemieva (2023) suggested that continental lithosphere can stretch to the point of spreading only if the subduction angle exceeds 45° and the subducting plate is older than 40 Ma, and that it also depends on its rheological weakness, controlled by temperature and hydration. Additionally, numerical models suggest that mantle flow around the wedge, due or not to slab break-off or slab windows, may further promote extension (Artemieva, 2023 and references therein). In the case of the North Patagonian margin, the subducting oceanic lithosphere is at least 150 Ma old, given the Cambrian separation of Cuyania and Chilenia from Laurentia (Thomas and Astini, 2003; Hyppolito et al., 2014a). Also, inherited crustal thinning from Cambrian rifting (Rapela et al., 2003) and the presence of a melting zone associated with the San Martín arc, active since at least 415 Ma (Rapela et al., 2021), may have reduced the North Patagonian lithospheric viscosity, aided by slab-derived fluids. Rapela et al. (2021) proposed that extension occurred in the forearc, an area already weakened by prior passive margin extension. The opening and closure of the Chaitenia BAB have been interpreted within an accretionary orogen context, involving repeated cycles of extension and compression rather than allochthonous terrane collision, driven by changes in slab geometry (Cawood et al., 2009; Rapela et al., 2021; Rapela et al., 2024). However, given the apparent temporal and spatial overlap with the Chilenia collision, it is possible that this tectonic event contributed to the Chaitenia orogenic cycle. We explore this potential link through two hypothetical models (Fig. 15), corresponding to the two subduction polarities discussed in Section 5.3.3—either directed toward the actual west or the east.

In the first model, the western Cuyanian margin is subducting towards the paleo SW beneath the eastern edge of Chilenia (Fig. 15a). This polarity contrasts with the paleo NE-dipping subduction beneath the North Patagonian margin (San Martín Arc; Rapela et al., 2021). We propose that both subduction zones were connected by a transform fault. Around 400 Ma, an oceanic domain existed southeast of the North Patagonian Massif – which will close later during Carboniferous accretion of South Patagonia as recorded by the S-type Chubut granite (Pankhurst et al., 2006) – and the possible connection with the subduction zone beneath South Patagonia and Antarctica would be via transform faults (Uriz et al., 2022; Riley et al., 2023). We thus suggest that the subduction segment along Northern Patagonia terminated at its southeastern edge. As the basin between Cuyania and Chilenia closed, the transform fault reoriented to accommodate plate motion—initially aligning both subduction zones, later acting as a dextral transfer zone during the Chilenia–Cuyania collision and Chaitenia BAB opening (Fig. 15b). In this setting, the short length of the North Patagonian subduction zone would promote toroidal mantle flow at its lateral edges, enhancing slab rollback and return flow (Schellart et al., 2007) (Fig. 15e). This would favor asthenospheric upwelling and stretching of the overriding plate. Analogous small, curved, retreating back-arc basins occur in ocean–ocean settings like the Scotia and Lesser Antilles (Schellart et al., 2007). A closer analogue for this model with opposing subduction directions is the Okinawa Trough, a BAB at the edge of continental Eurasia, north of the Taiwan orogen (Sibuet and Hsu, 2004). Several studies proposed that the Taiwan orogen helped initiate the lateral forearc extension and BAB formation in Okinawa (Letouzey and Kimura, 1984; Wallace et al., 2009).

In the second model, Chilenia is descending towards the paleo NE beneath the Cuyanian margin. In this scenario, the closure of the basin between Chilenia and Cuyania occurred with the same polarity as the subduction responsible for the San Martín Arc along the North Patagonian margin (Fig. 15c), implying both segments formed part of a continuous subduction zone—terminating in the southeast and leading to continental collision in the northwest. In this setting, the opening of the Chaitenia BAB could result from two main mechanisms. First, toroidal mantle flow and trench retreat may develop at the lateral edges of slabs of intermediate length, while the central segment remains stagnant—similar to the present-day Melanesia and NW Pacific subduction zones (Schellart et al., 2007). In this model, such flow would concentrate near the southeastern North Patagonian margin (Fig. 15d,f). Second, highly curved slabs in the transition zone between collision and subduction may develop slab tears (Fig. 15f), enabling mantle inflow that enhances trench retreat—an effect numerically modeled for the Mediterranean BABs (Magni et al., 2014). These authors emphasized that lateral collisions, where trench advance in the collision zone

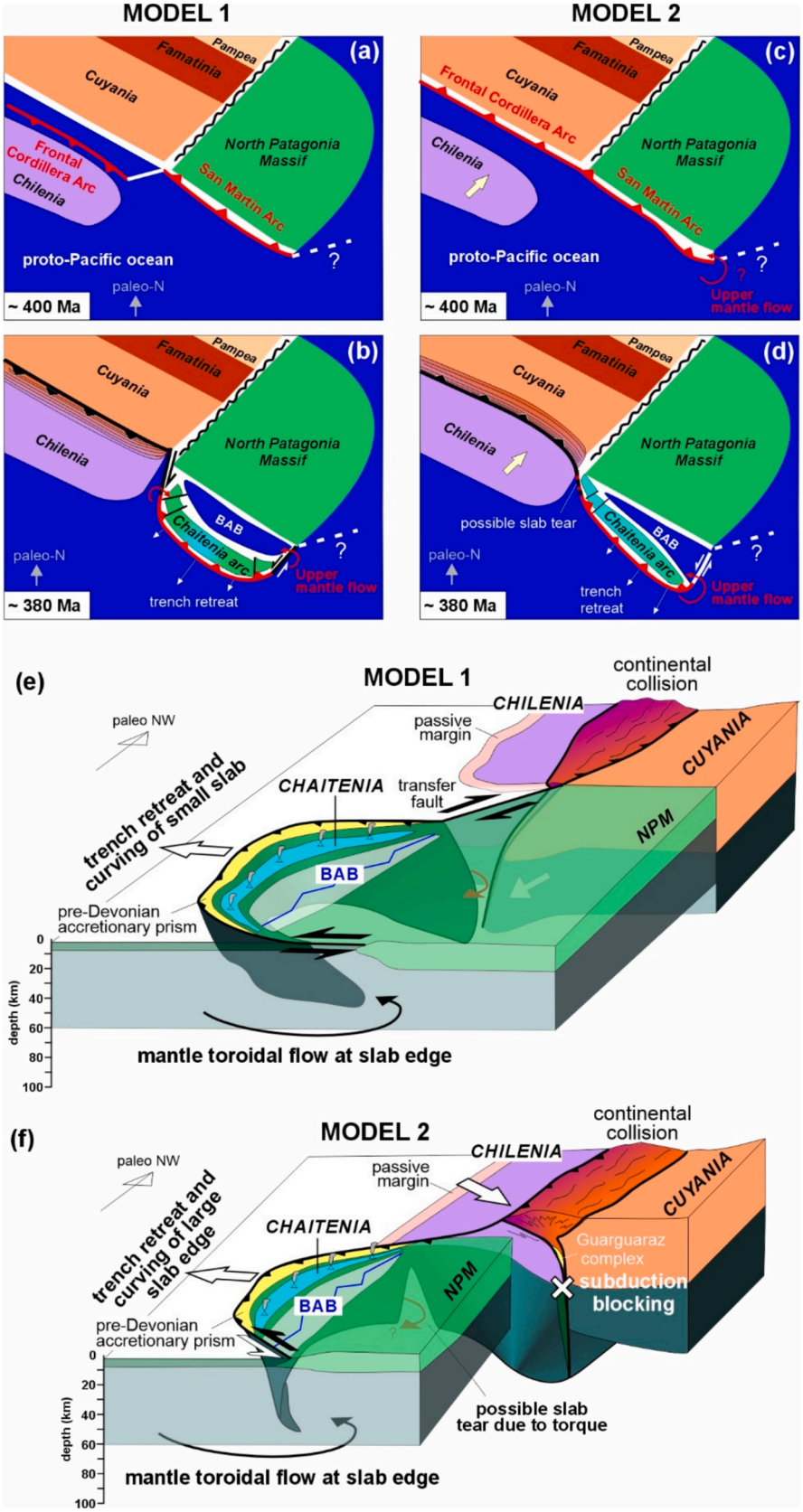

Fig. 15. Two models for the Chilenia collision inducing the formation of the Chaitenia oceanic arc and back-arc system at ~ 390–380 Ma. Map view (Up) and 3D (Down). **(a) (b) (e)** Model 1 with westwards vergence of collision. **(c) (d) (f)** Model 2 with eastwards vergence of collision. Both models will favor the opening of a back-arc in the overriding plate laterally to the orogen, in the North Patagonian Massif. Note the thin crust of the North Patagonian Massif. See test for explanations.

contrasts with retreat in the adjacent subduction segment, can promote stretching of both the overriding plate and the slab, creating pathways for mantle flow. As reviewed by Mantovani et al. (2001) and supported by GPS and paleomagnetic data (Wallace et al., 2009), most active BABs form near collision zones involving forearc rotation. These collision zones need not involve a continental indenter; buoyant oceanic features such as seamounts, plateaus, or arcs can also act as asperities (Wallace et al., 2005). Interestingly, the only modern examples of BABs forming within continental lithosphere—the Aegean Sea and Okinawa Trough—are both located adjacent to active collisional margins. Lastly, 3D thermo-mechanical models have successfully reproduced BAB development in such settings, confirming the viability of these mechanisms (Wallace et al., 2009; Hertgen et al., 2020).

In both tectonic models presented, the along-strike transition from collision to subduction appears to have played a key role in enabling the opening of the Chaitenia back-arc basin. Rather than acting as the sole mechanism, this configuration likely facilitated a set of reinforcing processes—including slab pull, slab curvature, potential slab tearing, toroidal mantle flow, rollback, and asthenospheric upwelling. These processes, combined with pre-existing weaknesses along the North Patagonian margin—such as inherited crustal thinning, elevated thermal gradients from arc magmatism (San Martín Arc), and hydration from slab-derived fluids—would have promoted extension of the overriding plate and trench retreat. However, geological evidence for this mechanism is limited today. No significant arc migration is observed between the San Martín (401 Ma) and Colán-Conhue (395 Ma) intrusions (Rapela et al., 2021), and no clear oroclinal features are preserved along the proposed edges of Chilenia. Orocline formation depends on convergence rate, duration of collision, and the presence of asperities (Marshak, 1988), and is less likely in narrow, elongated blocks such as Chilenia (~1000 km long, relatively narrow, and possibly lacking promontories). Comparable blocks like Cuyania also show no oroclinal structures in the Famatinian and Pampean domains. If the Chaitenia back-arc extended as far north as 38°S, the associated curvature—whether westward or eastward—would correspond to regions in the northern Neuquén Basin and adjacent Cordillera, where no relevant rocks are currently exposed. Furthermore, the closure of the Chaitenia basin and subsequent collision likely overprinted or destroyed any earlier oroclinal structures, which may also have been affected by later deformation events. Even if exposures of the relevant early Paleozoic rocks were available, recognizing such ancient curvature features would remain extremely challenging.

5.4.2. Paleogeographic reconstruction

From the above interpretations, we propose a revised paleogeographic reconstruction for the evolution of the SW margin of Gondwana. In this reconstruction (Fig. 16), we first consider that at ca. 400 Ma this margin was composed of the previously accreted Cuyania terrane and the North Patagonia Massif attached prior to early Paleozoic (Fig. 16a). The reconstruction is sketched for our second tectonic model, with collision of Chilenia towards the actual east, but this has no consequences for what would be happening at the latitudes of the Chaitenia arc and back-arc system. Thus, a subduction zone extended along the coastline (Fig. 16b), with the corresponding continental arc evidenced by the Rodeo de la Bordalesa, La Menta and Borborán intrusions in Cuyanian terrains in Argentina (Cingolani and Ramos, 2017) and the San Martín-Colán Conhue Arc in the North Patagonian zone (Hervé et al., 2018; Rapela et al., 2021). This subduction led to the collision of the Laurussia-derived, Chilenia terrane with the continental margin at about 385 Ma (e.g. Willner et al., 2011; Hyppolito et al., 2014a) (Fig. 16c). As a result, the North Patagonia margin extended, opening the Chaitenia back-arc with oceanic lithosphere (Fig. 16c). In this setting, the protoliths of the Guzmán and Los Pabilos amphibolites, of the San Carlos blueschists and of the La Cabaña ultramafic rocks (harzburgites, dunites and chromitites) formed (Fig. 16c). At this stage, the accretionary prism west of the Chaitenia oceanic arc was already well-developed, inherited from the previous 400 Ma active continental margin.

The back-arc domain began to close at ~ 375 Ma (Fig. 16d), as suggested by the presence of the Curruhué Cáceres Arc in the North Patagonia Massif (Rapela et al., 2021). Subduction initiation in this basin probably began at a density contrast and weak zone, such as a transform zone (Stern and Gerya, 2018; Ritter et al., 2024) or a past detachment fault at the transition between the continental and the oceanic back-arc (Lallemand and Arcay, 2021). Plate motion would have pushed towards the east and the former dextral transfer fault was likely reactivated as sinistral. Between 375 and 360 Ma (Fig. 16d), a double subduction towards the east was thus present west of the North Patagonian massif, as recognized by Rapela et al. (2021) with the Lago Yelcho intrusion as the Chaitenia oceanic arc in the Pacific domain and the Curruhué-Cáceres intrusions as the continental arc in the Foreland domain. In this scheme, the protoliths of the La Cabaña ultramafic rocks were located in the hanging wall of the back-arc subduction. The closure of the back-arc probably began in its southern part (Fig. 16d), as the Los Pabilos *retro*-eclogites (peak of 1.0–1.4 GPa and 500–550 °C; Kato et al., 2008) were already formed at ~ 360 Ma (Kato et al., 2008), whereas at the latitudes of the Guzmán area the protoliths of the garnet-bearing amphibolites and La Cabaña olivine-bearing antigoritites only initiated their subduction. At a larger scale, the subduction zone probably already extended to the south around the North Patagonia Massif (Fig. 16d), thus explaining the later collision of South Patagonia in Carboniferous times.

At 340–325 Ma (Fig. 16e), the closure of the Chaitenia back-arc was complete. The two subduction zones joined and the thermal structure in the northern part, inherited from the previous back-arc system, was still characterized by a very hot hanging wall. The Guzmán amphibolites and La Cabaña olivine-bearing antigoritites reached their peak metamorphism at about 650 °C and 0.9–1.3 GPa (30–45 km depth) (Fig. 12, Fig. 16e). The registered hot metamorphic gradient thus results from the beginning of the subduction, not initiated in the context of a passive continental margin but in a back-arc setting. This could explain the higher temperatures registered in the Guzmán amphibolites in comparison with classical subduction onset paths like Punta Sirena (Hyppolito et al., 2014b). Meanwhile, in the southern part of the closed back-arc (Fig. 16e), the subduction system already reached a more mature thermal configuration, as showed by the formation of the San Carlos blueschists at ~ 335 Ma (Fig. 13) and blueschist overprint on the Los Pabilos *retro*-eclogites at 325 Ma (Kato et al., 2008). The 340–330 Ma period seems to represent a major turning point for this zone of the SW Gondwanan margin. The E-directed subduction propagated northwards, as registered by the Punta Sirena amphibolites (Hyppolito et al., 2014b) and the El Volcán arc granite (Creixell et al., 2021) (Fig. 16e). The Bariloche granite, interpreted by Pankhurst et al. (2006) as produced by the northwards subduction of the oceanic basin between North Patagonia and South Patagonia, could also result from the N propagation of the E-directed subduction.

At 320–290 Ma (Fig. 16f), this subduction configuration all along the coast caused the emplacement of the Coastal Batholith Arc (Deckart et al., 2014; Creixell et al., 2021). The collision of the Chaitenia oceanic arc with the North Patagonian massif continued, probably enhanced by the northwards directed collision of South Patagonia with the southern edge of the North Patagonia Massif, evidenced by the presence of the S-type Chubut granite (Pankhurst et al., 2006). At ~ 320 Ma, the Guzmán amphibolites and La Cabaña olivine-bearing antigoritites probably began their exhumation in the subduction channel (Fig. 16f), between Stages 2 and 3 of their *P–T* path (Fig. 12). Southwards, the San Carlos blueschists were probably also incorporated in the subduction channel, but in a zone with very slow exhumation (high-*P* retrograde portion of Stage 2, Fig. 13). At ~ 310–290 Ma, the E-directed subduction zone became mature in its more northern part, with isotherms displacing to higher depths, as recorded in the Pichilemu blueschists (0.8–1.1 GPa and 380–420 °C; Willner et al., 2005, Muñoz-Montecinos et al., 2020) with OIBs signatures derived from seamounts (Hyppolito et al., 2014a;

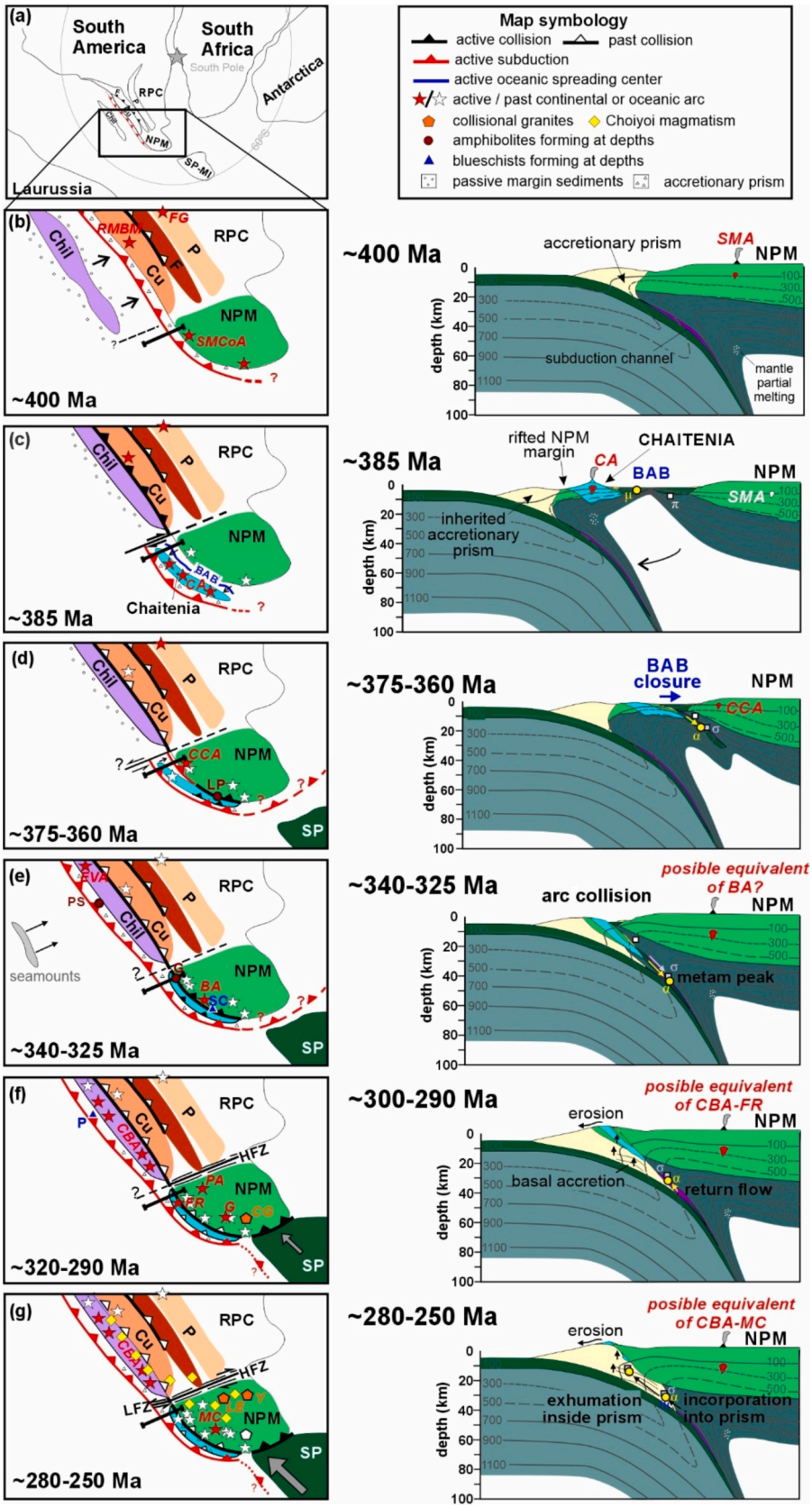

(caption on next page)

Fig. 16. Model for the evolution of the SW Gondwanan margin from 400 to 250 Ma. Left: Schematic paleogeographic maps of the southern edge of Gondwana, displaying subduction zones, terranes movements and collision. Principal registered arcs are located, as well as metamorphic records of amphibolites and blueschists. Right: Schematic cross-sections and thermal configuration for the La Cabaña-Guzmán sector (location indicated in maps), highlighting the evolution of mafic and ultramafic rocks. Note that a similar evolution would occur in the southern part of the back-arc (San Carlos-Manquemapu and Los Pabilos sectors), but earlier, as the closure of the back-arc would begin there. **(a)** 400 Ma. Localization of the zone in the frame of Gondwana. Plate reconstruction taken from Torsvik and Cocks (2013). **(b)** 400 Ma. Zoom on the southern edge of South America, displaying a subduction zone along Cuyania and NPM, and Chilenia approaching. **(c)** 385 Ma. Collision of the Chilenia indenter and opening of the Chaitenia back-arc basin from the NPM margin. Formation of the protoliths of Guzmán, San Carlos and Los Pabilos mafic rocks (μ) and La Cabaña peridotites (π) in the BAB. **(d)** 375–360 Ma. Closure of the BAB with onset of double subduction system and collision of the Chaitenia oceanic arc beginning to the south. Formation of the Los Pabilos eclogites and amphibolites (α). **(e)** 340–325 Ma. Complete collision of Chaitenia oceanic arc and end of the double subduction. Propagation of the subduction to the north along Chilenia. Cold metamorphic peak of San Carlos blueschists and hot metamorphic peak of Guzmán amphibolites and La Cabaña olivine-bearing antigoritites. **(f)** 320–290 Ma. Active continental margin along the western coast of South Gondwana. Collision of the South Patagonia terrane with the NPM. Return flow of the San Carlos blueschists and Guzmán amphibolites (α) in the subduction channel. Formation of the Pichilemu blueschists in the north. **(g)** 280–250 Ma. Active continental margin. Hydration event of Guzmán amphibolites during incorporation in the prism. Retrograde event of the San Carlos blueschists near the base of the accretionary prism followed by exhumation of the mafic rocks inside the prism. Abbreviations of blocks: Chil: Chilenia. Cu: Cuyania. F: Famantinian arc. NPM: North Patagonian Massif. P: Pampea. RPC: Rio de la Plata Craton. SP-MI: South Patagonia-Malvinas Islands. Abbreviations of plutonic rocks: BA: Bariloche Arc (Pankhurst et al., 2006), CBA: Coastal Batholith Arc (Deckart et al., 2014; Creixell et al., 2021), CCA: Curruhué Cáceres Arc (Rapela et al., 2021), CG: Chubut collisional granites (Pankhurst et al., 2006), EVA: El Volcan Arc (Creixell et al., 2021), FG: Foreland Granites (Dahlquist et al., 2021), FR: Futrono Rinihue pluton (Deckart et al., 2014), LE and Y: La Esperanza and Yaminue plutons (Pankhurst et al., 2006; Castillo et al., 2017), MC: Mamil Choique pluton (Pankhurst et al., 2006; Castillo et al., 2017), PA and G: Piedra Aguila and Gastre plutons (Pankhurst et al., 2006; Castillo et al., 2017), RBMB: Rodeo de la Bordalesa, Menta and Borborán intrusions (Cingolani and Ramos, 2017), SMCoA: San Martín Colán Conhue Arc (Hervé et al., 2018; Rapela et al., 2021). Abbreviations of subduction-related metamorphic rocks: G: Guzmán amphibolites (this study), SC: San Carlos blueschists (this study), LP: Los Pabilos *retro*-eclogites and blueschists overprint (Kato et al., 2008), P: Pichilemu blueschists (Willner et al., 2005; Hyppolito et al., 2014a), PS: Punta Sirena amphibolites (Hyppolito et al., 2014b).

Muñoz-Montecinos et al., 2024). The La Cabaña-Guzmán area acquired thermal maturity slightly later due to the inheritance of the hot back-arc architecture. Thus, at 311–299 Ma, the Guzmán amphibolites were still retrograding, cooling down to 500 °C at ~ 1.0 GPa nearly reaching Stage 3 of Fig. 12. As for the southern San Carlos blueschists, they began their exhumation in the subduction channel (between Stage 2 and 3, Fig. 13). The continental arc was still highly active as supported by the development of the Coastal Batholith (Creixell et al., 2021), the Futrono-Rinihue granite (Deckart et al., 2014), and the Piedra Aguila and Gastre granites (Pankhurst et al., 2006; Castillo et al., 2017) (Fig. 16f). The northwestward push of South Patagonia generated deformation and metamorphism in the weak zone (Pre-early Paleozoic suture?) located between the Cuyania-Famatinia-Pampea block and the North Patagonian Massif (Pankhurst et al., 2006). This event could have activated the Huincul Fault Zone. Besides, this NW-directed push combined with the E-directed subduction could explain the transpressional deformation observed in Argentina in the North Patagonian Cordillera (Oriolo et al., 2019).

At 280–270 Ma (Fig. 16g**g**), the global geodynamic setting remained the same, the Coastal Batholith Arc being still active as evidenced by the formation of the Mamil Choique complex in the South Patagonian massif (Pankhurst et al., 2006; Castillo et al., 2017). At that time, the Guzmán meta-mafic rocks experienced the hydration event of Stage 3 (Fig. 12), when they were emplaced in the tail of the accretionary prism (500 °C at ~ 0.9–1.0 GPa) together with the La Cabaña ultramafic rocks (Romero et al., 2017; Höfer et al., 2001) (Fig. 16g). Southwards, the San Carlos blueschists reached the base of the accretionary prism with retrogradation in the greenschist facies (Stage 3). Also, in this period the Lanalhue Fault Zone may have developed in semi-ductile conditions as sinistral inside the accretionary prism (Glodny et al., 2008), possibly reactivating the fault previously accommodating the opening and closure of the Chaitenia back-arc.

Finally, at 250 Ma, the subduction was still active along the SW Gondwanan margin (Oliveros et al., 2020; Creixell et al., 2021) (Fig. 16g). At that time, the Guzmán, San Carlos and Los Pabilos meta-mafic rocks exhumed inside the prism. Moreover, in this period the La Esperanza granite and rhyolite and Yaminue collisional plutons in the North Patagonian massif formed in a compressional setting (Pankhurst et al., 2006; Castillo et al., 2017), interpreted by Oriolo et al. (2023) as related to an accretionary orogeny advancing towards the east due to slab shallowing, resulting in a thickened crust (Oriolo et al., 2023). Also, a new South Patagonia push could have reactivated the Huincul Fault Zone as dextral (Gregori et al., 2008). At a larger scale, this special configuration with two orthogonal slabs undergoing break-off (one from the E-directed subduction zone and the other from the N-directed collision of South Patagonia) would be responsible for the significant Choiyoi magmatism from Northern Chile to the North Patagonian massif (Fig. 16g), emplaced in an extensional regime at 280–250 Ma, far away from the paleo-trench and suture zone (Gianni and Navarrete, 2022).

6. Conclusions

We studied the tectono-metamorphic evolution of newly discovered mafic rocks incorporated in the Chilean paleo-prism in two sectors (Guzmán and San Carlos-Manquemapu) that record distinct *P–T–t* paths. The Guzmán retrogressed garnet-bearing amphibolites recorded a counterclockwise metamorphic path consisting of four stages: 1) a prograde event, only preserved inside garnet cores as incomplete consumption of ilmenite to rutile; 2) a metamorphic peak at ~ 650 °C /1.0–1.2 GPa forming the paragenesis of Grt I + Pl + Hbl + Ep + Rt; 3) a nearly isobaric retrograde hydration event at 480–520 °C / 0.8–1.1 GPa, forming the paragenesis of Grt II + Ep + Act + Chl + Ttn ± Bt and; 4) a final retrograde event at lower temperatures from 400 to 330 °C. New *in situ* amphibole $^{40}Ar/^{39}Ar$ dating reveals three age populations that are integrated in the metamorphic trajectory as follows. The peak conditions suggest that the rocks followed a hot *P–T* path, when the subduction system was still thermally immature and reached depths of ca. 35–40 km probably at ~ 340 Ma. There, samples cooled down nearly isobarically and passed the hornblende closure temperature of 500 °C at 311–299 Ma. They were later affected by the hydration event of stage 3 at 277–270 Ma (actinolite crystallization) at depths of 30–35 km. This age, which is similar within error to ages obtained in fuchsite from host metasediments and metasomatic zircons from the La Cabaña blackwall, likely corresponds to the emplacement of the mafic and ultramafic rocks from the studied area inside the deep tail of the sedimentary prism. Finally, our youngest amphibole ages (ca. 250–240 Ma) registered actinolite recrystallization during exhumation in the prism.

The San Carlos-Manquemapu blueschists recorded a hairpin path consisting of three main stages: 1) a prograde event, preserved in Grt1 zoning, Ca-rich glaucophane cores and Fe-rich epidote cores; 2) a metamorphic peak at ~ 1.6 GPa – 450 °C and a subsequent high-*P* retrograde event, forming the paragenesis of Grt 2 + Gln(rim) + WM1 + Ep(rim) + Ttn + Rt; and 3) a retrograde path associated to exhumation down to ~ 0.7 GPa – 350 °C. New *in situ* phengite $^{40}Ar/^{39}Ar$ dating reveals four age populations that are integrated in the metamorphic trajectory as follows. The peak conditions suggest that the rocks followed a

cold *P–T* path, when the subduction system already had a mature thermal configuration. The rocks reached depths of 55 km, where WM1a phengites crystallized at ~ 335 Ma. This is in agreement with previous ages obtained for the blueschist overprint on the *retro*-eclogites of Los Pabilos. At ~ 295 Ma, the San Carlos blueschists begun a slow exhumation in the subduction channel, as showed by the crystallization of WM1b phengites. They further continued in the channel up to the base of the accretionary prism at ~ 267 Ma, where they underwent a retrograde greenschist metamorphism. Finally, younger age population of ~ 220 Ma corresponds to recrystallization inside the prism.

Our geochemical results on the mafic rocks sampled in the three studied sectors of Guzmán, San Carlos-Manquemapu and Los Pabilos suggest that they originated in a back-arc setting. We thus consider that the Chaitenia back-arc system continued northwards with the Lanalhue fault as limit, due to the lack of oceanic arc-derived signatures in mafic rocks north of this fault. This northern limit also coincides in latitudes with the southern border of Chilenia. We propose that the formation of the Chaitenia oceanic arc and the opening of the Chaitenia back-arc in the North Patagonian massif were due to a roll-back induced south of the collision zone between Chilenia and the SW Gondwanan margin. The back-arc closed at 380–375 Ma, generating a double subduction configuration. The distinct *P–T–t* paths between San Carlos and Guzmán sectors account for a diachronic thermal evolution of the subduction system, with closure beginning in its southern part. Indeed, the hairpin *P–T* path of the San Carlos blueschists points to a thermal mature configuration at 335 Ma in the south whereas the counterclockwise *P–T* path of the Guzmán amphibolites records, for a same period in the north, a hot prograde path and thermal architecture inherited from subduction initiation in a back-arc setting. The basin completely closed at 340–330 Ma with the reestablishment of a continental arc and the northwards propagation of the subduction zone on the western margin of the previously accreted Chilenia.

CRediT authorship contribution statement

Gaëlle Plissart: Writing – review & editing, Writing – original draft, Visualization, Validation, Supervision, Resources, Project administration, Methodology, Investigation, Funding acquisition, Formal analysis, Data curation, Conceptualization. **Juan Carlos Moral Yilorm:** Writing – review & editing, Validation, Resources, Methodology, Investigation, Formal analysis, Data curation. **José María González-Jiménez:** Writing – review & editing, Resources, Investigation, Funding acquisition. **Jesús Muñoz-Montecinos:** Writing – review & editing, Validation, Methodology, Investigation, Formal analysis. **Carolina Pavez Salgado:** Resources, Investigation, Formal analysis, Data curation. **Aníbal Rivera Herrera:** Resources, Investigation, Formal analysis, Data curation. **Fiona Cabrera Bermúdez:** Investigation, Formal analysis, Data curation. **Claudio Marchesi:** Writing – review & editing, Supervision, Resources, Investigation. **Alexandre Corgne:** Writing – review & editing, Supervision, Investigation. **Antonio Jesús Moreno Abril:** Investigation, Formal analysis. **Pierre Lanari:** Writing – review & editing, Software. **Julien Berger:** Writing – review & editing, Resources, Investigation. **Alison Halton:** Writing – review & editing, Validation, Resources, Methodology, Formal analysis.

Declaration of competing interest

The authors declare that they have no known competing financial interests or personal relationships that could have appeared to influence the work reported in this paper.

Acknowledgements

We thank the associate editor D. Nance and the reviewers Dr. Heinrich Bahlberg, Dr. Carlos Rapela and Dr. Joaquín Bastías for their valuable comments and suggestions that significantly improved the manuscript. We also thank our colleagues D. Melnick and M. Schilling for insightful discussion on a first version of this manuscript. This work was supported by Fondecyt Iniciación Grants (#11150635 and #11140005), and the RYC-2015-17596 to José Maria González-Jiménez. We also acknowledge Laurent Lenta (University of Nantes) and Jesús Montes-Rueda (University of Granada) for their careful preparation of thin sections, Philippe De Parseval and Sophie Gouy (Centre de Microcaractérisation Raimond Castaing) for assistance during EMPA work and Ricardo Silva for SEM analyses (UACh).

Appendix A. Supplementary data

Supplementary data to this article can be found online at https://doi.org/10.1016/j.gr.2025.07.023.

References

Álvarez, J., Mpodozis, C., Arriagada, C., Astini, R., Morata, D., Salazar, E., Valencia, V.A., Vervoort, J.D., 2011. Detrital zircons from late Paleozoic accretionary complexes in north-central Chile (28°-32°S): possible fingerprints of the Chilenia terrane. J. S. Am. Earth Sci. 32, 460–476. https://doi.org/10.1016/j.jsames.2011.06.002.

Artemieva, I.M., 2023. Back-arc basins: a global view from geophysical synthesis and analysis. Earth Sci. Rev. 236, 104242. https://doi.org/10.1016/j.earscirev.2022.104242.

Ayres, M., Vance, D., 1997. A comparative study of diffusion profiles in Himalayan and Dalradian garnets: constraints on diffusion data and the relative duration of the metamorphic events. Contrib. Mineral. Petrol. 128, 66–80. https://doi.org/10.1007/s004100050294.

Barra, F., Rabbia, O.M., Alfaro, G., Miller, H., Höfer, C., Kraus, S., 1998. Serpentinitas y cromititas de La Cabaña, Cordillera de la Costa Chile Central. Revista Geológica De Chile 25 (1). https://doi.org/10.4067/S0716-02081998000100003.

Boedo, F.L., Pérez Luján, S., Naipauer, M., Vujovich, G.I., Pimentel, M.M., Ariza, J.P., Barredo, S.P., 2020. The late Neoproterozoic-early Paleozoic basin of the western Argentine Precordillera: insights from zircon U-PB geochronology. J. South Am. Earth Sci. 102669. https://doi.org/10.1016/j.jsames.2020.102669.

Boedo, F.L., Pérez Luján, S., Ariza, J.P., Vujovich, G.I., 2021. The mafic-ultramafic belt of the Argentine Precordillera: a geological synthesis. J. South Am. Earth Sci. 110, 103354. https://doi.org/10.1016/j.jsames.2021.103354.

Cabbanis, B., Lecolle, M., 1989. Le diagramme La/10–Y/15–Nb/8: Un outil pour la discrimination des series volcaniques et la mise en evidence des processus de mélange et/ou de contamination crustale. C. R. Acad. Sci Series II 309, 2023–2029.

Castillo, P., Fanning, C.M., Pankhurst, R.J., Hervé, F., Rapela, C.W., 2017. Zircon O- and Hf-isotope constraints on the genesis and tectonic significance of Permian magmatism in Patagonia. J. Geol. Soc. 174, 803–816. https://doi.org/10.1144/jgs2016-152.

Cathelineau, M., 1988. Cation site occupancy in chlorites and illites as a function of temperature. Clay Mineral. 23, 471–485.

Cawood, P.A., Kröner, A., Collins, W.J., Kusky, T.M., Mooney, W.D., Windley, B.F., 2009. Accretionary orogens through Earth history. Geol. Soc. Special Publication 318 (1), 1–36. https://doi.org/10.1144/SP318.1.

Cingolani, C.A., Ramos, V.A., 2017. Pre-carboniferous tectonic evolution of the san Rafael block, Mendoza province. In: Cingolani, C.A. (Ed.), Pre-Carboniferous Evolution of the San Rafael Block, Argentina: implications in the SW Gondwana Margin. Springer Earth System Sciences, 239–255. Doi: 10.1007/978-3-319-50153-6_13.

Connolly, J.A.D., 2009. The geodynamic equation of state: what and how: geodynamic equation of state-what and how. Geochem. Geophys. 10 (10), n/a-n/a. https://doi.org/10.1029/2009GC002540.

Creixell, C., Sepúlveda, F., Álvarez, J., Vásquez, P., Velásquez, R., 2021. The carboniferous onset of subduction at SW Gondwana revisited: Sedimentation and deformation processes along the late Paleozoic forearc of north Chile (21°–33° S). J. South Am. Earth Sci. 107, 103149. https://doi.org/10.1016/j.jsames.2020.103149.

Dahlquist, J.A., Morales Cámera, M.M., Alasino, P.H., Tickyj, H., Basei, M.A.S., Galindo, C., Moreno, J.A., Rocher, S., 2020. Geochronology and geochemistry of Devonian magmatism in the Frontal cordillera (Argentina): geodynamic implications for the pre-andean SW Gondwana margin. Int. Geol. Rev. 64 (2), 233–253. https://doi.org/10.1080/00206814.2020.1845994.

Dahlquist, J.A., Morales Cámera, M.M., Alasino, P.H., Pankhurst, R.J., Basei, M.A.S., Rapela, C.W., Moreno, J.A., Baldo, E.G., Galindo, C., 2021. A review of Devonian-Carboniferous magmatism in the central region of Argentina, pre-andean margin of SW Gondwana. Earth Sci. Rev. 221, 103781. https://doi.org/10.1016/j.earscirev.2021.103781.

Davis, J.S., Roeske, S., McClelland, W., Snee, L., 1999. Closing the ocean between the Precordillera terrane and Chilenia: early Devonian ophiolite emplacement and deformation in the southwest Precordillera. In: Ramos, V.A., Keppie, J.D. (Eds.), Laurentia-Gondwana Connection before Pangea, vol. 336. Geol. Soc. Am. Special Publication 336, 115–138. DOI: 10.1130/0-8137-2336-1.115.

Davis, J.S., Roeske, S.M., McClelland, W.C., Kay, S., 2000. Mafic and ultramafic crustal fragments of the southwestern Precordillera terrane and their bearing on tectonic

models of the early Paleozoic in western Argentina. Geology 28 (2), 171–174. https://doi.org/10.1130/0091-7613(2000)28<171:MAUCFO>2.0.CO;2.
Deckart, K., Hervé, F., Fanning, C.M., Ramírez, V., Calderón, M., Godoy, E., 2014. Geocronología U-Pb e isótopos de Hf-O en circones del batolito de la Costa Pensilvaniana Chile. Andean Geol. 41 (1), 49–82. https://doi.org/10.5027/andgeoV41n1-a03.
Diener, J.F.A., Powell, R., 2012. Revised activity-composition models for clinopyroxene and amphibole: REVISED A-x MODELS FOR CPX & AMPHIBOLE. J. Metamorph. Geol. 30 (2), 131–142. https://doi.org/10.1111/j.1525-1314.2011.00959.x.
Dilek, Y., Furnes, H., 2011. Ophiolite genesis and global tectonics: geochemical and tectonic fingerprinting of ancient oceanic lithosphere. Geol. Soc. Am. Bull. 123 (3–4), 387–411. https://doi.org/10.1130/B30446.1.
Donoso-Tapia, D., Flores, K.E., Martin, C., Gazel, E., Marsh, J., 2024. Exhumed serpentinites and their tectonic significance in non-collisional orogens. Geochem. Geophys. 25 (2), e2023GC011072. https://doi.org/10.1029/2023GC011072.
Duhart, P., McDonough, M., Muñoz, J., Martin, M., Villeneuve, M., 2001. El Complejo Metamórfico Bahía Mansa en la cordillera de la Costa del centro-sur de Chile (39°30′-42°00′S): geocronología K-Ar, 40Ar/39Ar y U-Pb e implicancias en la evolución del margen sur-occidental de Gondwana. Revista Geológica De Chile 28 (2). https://doi.org/10.4067/S0716-02082001000200003.
Ernst, W.G., Liu, J., 1998. Experimental phase-equilibrium study of Al- and Ti-contents of calcic amphibole in MORB; a semiquantitative thermobarometer. Amer. Miner. 83 (9–10), 952–969. https://doi.org/10.2138/am-1998-9-1004.
Frutos, J.J., Alfaro, H.G., 1987. Metallogenic and tectonic characteristics of the paleozoic ophiolitic belt of the southern Chile coastal Cordillera. Geol. Rundsch. 76 (2), 343–356. https://doi.org/10.1007/BF01821079.
García-Sansegundo, J., Gallastegui, G., Farias, P., Rubio-Ordóñez, Á., Cuesta, A., Heredia, N., Giambiagi, L., Clariana, P., 2016. Evolución tectono-metamórfica Chánica del Complejo Guarguaraz, Cordillera Frontal de los Andes (Mendoza, Argentina). Geotemas 16 (2), 427–430.
García-Sansegundo, J., Farias, P., Rubio-Ordóñez, Á., Clariana, P., Cingolani, C., Heredia, N., 2023. Polyorogenic structure of the San Rafael Block, Mendoza, Argentina: new data for the interpretation of the Chanic Orogen. J. South Am. Earth Sci. 124, 104277. https://doi.org/10.1016/j.jsames.2023.104277.
Giambiagi, L., Mescua, J., Heredia, N., Farías, P., García Sansegundo, J., Fernández, C., Stier, S., Pérez, D., Bechis, F., Moreiras, S.M., Lossada, A., 2014. Reactivation of Paleozoic structures during Cenozoic deformation in the Cordón del Plata and Southern Precordillera ranges (Mendoza, Argentina). J. Iberian Geol. 40 (2), 309–320. https://doi.org/10.5209/rev_JIGE.2014.v40.n2.45302.
Gianni, G.M., Navarrete, C.R., 2022. Catastrophic slab loss in southwestern Pangea preserved in the mantle and igneous record. Nat. Commun. 13, 698. https://doi.org/10.1038/s41467-022-28290-z.
Glodny, J., Lohrmann, J., Echtler, H., Gräfe, K., Seifert, W., Collao, S., Figueroa, O., 2005. Internal dynamics of a paleoaccretionary wedge: Insights from combined isotope tectonochronology and sandbox modelling of the South-Central Chilean forearc. Earth Planet. Sci. Lett. 231 (1–2), 23–39. https://doi.org/10.1016/j.epsl.2004.12.014.
Glodny, J., Echtler, H., Collao, S., Ardiles, M., Burón, P., Figueroa, O., 2008. Differential late Paleozoic active margin evolution in South-Central Chile (37°S–40°S) – the Lanalhue Fault Zone. J. South Am. Earth Sci. 26 (4), 397–411. https://doi.org/10.1016/j.jsames.2008.06.001.
González-Jiménez, J.M., Barra, F., Walker, R.J., Reich, M., Gervilla, F., 2014. Geodynamic implications of ophiolitic chromitites in the La Cabaña ultramafic bodies Central Chile. Int. Geol. Rev. 56 (12), 1466–1483. https://doi.org/10.1080/00206814.2014.947334.
González-Jiménez, J.M., Barra, F., Garrido, L., Reich, M., Satsukawa, T., Romero, R., Salazar, E., Colás, V., Orellana, F., Rabbia, O., Plissart, G., Morata, D., 2016. A secondary precious and base metal mineralization in chromitites linked to the development of a Paleozoic accretionary complex in Central Chile. Ore Geol. Rev. 78, 14–40. https://doi.org/10.1016/j.oregeorev.2016.02.017.
González-Jiménez, J.M., Plissart, G., Garrido, L.N., Padrón-Navarta, J.A., Aiglsperger, T., Romero, R., Marchesi, C., Moreno-Abril, A.J., Reich, M., Barra, F., Morata, D., 2017. Titanian clinohumite and chondrodite in antigorite serpentinites from Central Chile: evidence for deep and cold subduction. Eur. J. Mineral. 29 (6), 959–970. https://doi.org/10.1127/ejm/2017/0029-2668.
González-Jiménez, J.M., Piña, R., Saunders, J.E., Plissart, G., Marchesi, C., Padrón-Navarta, J.A., Ramón-Fernandez, M., Garrido, L.N.F., Gervilla, F., 2021. Trace element fingerprints of Ni–Fe–S–As minerals in subduction channel serpentinites. Lithos 400–401, 106432. https://doi.org/10.1016/j.lithos.2021.106432.
Graham, C.M., Powell, R., 1984. A garnet–hornblende geothermometer: calibration, testing, and application to the Pelona Schist, Southern California. J. Metamorph. Geol.
Gregori, D.A., Kostadinoff, J., Strazzere, L., Raniolo, A., 2008. Tectonic significance and consequences of the Gondwanide orogeny in northern Patagonia Argentina. Gondwana Res. 14, 429–450. https://doi.org/10.1016/j.gr.2008.04.005.
Halama, R., Konrad-Schmolke, M., 2015. Retrograde metasomatic effects on phase assemblages in an interlayered blueschist–greenschist sequence (Coastal Cordillera, Chile). Lithos 216–217, 31–47. https://doi.org/10.1016/j.lithos.2014.12.004.
Harrison, T.M., 1981. Diffusion of ^{40}Ar in hornblende. Contrib. Mineral. Petrol. 78, 329–331.
Harrison, T.M., Célérier, J., Aikman, A.B., Hermann, J., Heizler, M.T., 2009. Diffusion of 40Ar in muscovite. Geochim. Cosmochim. Acta 73, 1039–1051. https://doi.org/10.1016/j.gca.2008.09.038.
Hertgen, S., Yamato, P., Guillaume, B., Magni, V., Schliffke, N., van Hunen, J., 2020. Influence of the thickness of the overriding plate on convergence zone dynamics. Geochem. Geophys. 21, e2019GC008678. https://doi.org/10.1029/2019GC008678.
Hervé, F., 1988. Late paleozoic subduction and accretion in Southern Chile. Episodes 11 (3), 183–188. https://doi.org/10.18814/epiiugs/1988/v11i3/005.
Hervé, F., Calderón, M., Fanning, C.M., Pankhurst, R.J., Godoy, E., 2013. Provenance variations in the late Paleozoic accretionary complex of central Chile as indicated by detrital zircons. Gondwana Res. 23 (3), 1122–1135. https://doi.org/10.1016/j.gr.2012.06.016.
Hervé, F., Calderon, M., Fanning, C.M., Pankhurst, R.J., Fuentes, F., Rapela, C.W., Correa, J., Quezada, P., Marambio, C., 2016. Devonian magmatism in the accretionary complex of southern Chile. J. Geol. Soc. 173 (4), 587–602. https://doi.org/10.1144/jgs2015-163.
Hervé, F., Calderón, M., Fanning, M., Pankhurst, R., Rapela, C.W., Quezada, P., 2018. The country rocks of Devonian magmatism in the North Patagonian Massif and Chaitenia. Andean Geol. 45 (3), 301. https://doi.org/10.5027/andgeoV45n3-3117.
Höfer, C., Kraus, S., Miller, H., Alfaro, G., Barra, F., 2001. Chromite-bearing serpentinite bodies within an arc-backarc metamorphic complex near La Cabaña, south Chilean Coastal Cordillera. J. South Am. Earth Sci. 14. https://doi.org/10.1016/S0895-9811(01)00011-6.
Holdaway, M.J., 2000. Application of new experimental and garnet Margules data to the garnet-biotite geothermometer. Amer. Miner. 85, 881–892. https://doi.org/10.2138/am-2000-0701.
Holland, T., Powell, R., 2011. An improved and extended internally consistent thermodynamic dataset for phases of petrological interest, involving a new equation of state for solids. J. Metamorph. Geol. 29, 333–383. https://doi.org/10.1111/j.1525-1314.2010.00923.x.
Hollocher, K., Robinson, P., Walsh, E., Roberts, D., 2012. Geochemistry of amphibolite-facies volcanics and gabros of the Storen Nappe in extensions west and southwest of Trondheim, western gneiss región, Norway. A key to correlations and paleotectonic settings. Amer. J. Sci. 312, 357–416. https://doi.org/10.2475/04.2012.01.
Hyppolito, T., Juliani, C., García-Casco, A., Meira, V.T., Bustamante, A., Hervé, F., 2014a. The nature of the Palaeozoic oceanic basin at the southwestern margin of Gondwana and implications for the origin of the Chilenia terrane (Pichilemu region, central Chile). Int. Geol. Rev. 56 (9), 1097–1121. https://doi.org/10.1080/00206814.2014.919612.
Hyppolito, T., García-Casco, A., Juliani, C., Meira, V.T., Hall, C., 2014b. Late Paleozoic onset of subduction and exhumation at the western margin of Gondwana (Chilenia Terrane): Counterclockwise P–T paths and timing of metamorphism of deep-seated garnet–mica schist and amphibolite of Punta Sirena, Coastal Accretionary complex, central Chile (34° S). Lithos 206–207, 409–434. https://doi.org/10.1016/j.lithos.2014.07.023.
Jolivet, L., Tamaki, K., Fournier, M., 1994. Japan Sea, opening history and mechanism: a synthesis. J. Geophys. Res. 99 (B11), 22237–22259. https://doi.org/10.1029/93JB03463.
Kamzolkin, V.A., Ivanov, S.D., Konilov, A.N., 2016. Empirical Phengite Geobarometer: Background, Calibration, and Application. Geology of Ore Deposits 58 (8), 613–622. https://doi.org/10.1134/S1075701516080092.
Kaneko, Y., Miyano, T., 2004. Recalibration of mutually consistent garnet-biotite and garnet-cordierite geothermometers. Lithos 73 (3–4), 255–269. https://doi.org/10.1016/j.lithos.2003.12.009.
Kato, T.T., Sharp, W.D., Godoy, E., 2008. Inception of a Devonian subduction zone along the southwestern Gondwana margin: 40 Ar– 39 Ar dating of eclogite–amphibolite assemblages in blueschist boulders from the Coastal Range of Chile (41°S). Can. J. Earth Sci. 45 (3), 337–351. https://doi.org/10.1139/E08-006.
Kleemann, U., Reinhardt, J., 1994. Garnet-biotite thermometry revisited; the effect of Al [VI] and Ti in biotite. Eur. J. Miner. 6 (6), 925–941. https://doi.org/10.1127/ejm/6/6/0925.
Kostadinoff, J., Gregori, D.A., Raniolo, L.A., 2005. Configuración geofísica–geológica del sector Norte de la provincia de Río Negro. Revista De La Asociación Geológica Argentina 60, 368–376.
Kunz, B.E., White, R.W., 2019. Phase equilibrium modelling of the amphibolite to granulite facies transition in metabasic rocks (Ivrea Zone, NW Italy). J. Metamorph. Geol. 37, 935–950. https://doi.org/10.1111/jmg.12478.
Lallemand, S., Arcay, D., 2021. Subduction initiation from the earliest stages to self-sustained subduction: insights from the analysis of 70 Cenozoic sites. Earth Sci. Rev. 221, 103779. https://doi.org/10.1016/j.earscirev.2021.103779.
Lanari, P., Wagner, T., Vidal, O., 2014. A thermodynamic model for di–trioctahedral chlorite from experimental and natural data in the system MgO–FeO–Al2O3–SiO2–H2O: applications to P–T sections and geothermometry. Contrib. Mineral. Petrol. 167, 968. https://doi.org/10.1007/s00410-014-0968-8.
Lanari, P., Engi, M., 2017. Local bulk composition effects on metamorphic mineral assemblages. Rev. Miner. Geochem. 83, 55–102. https://doi.org/10.2138/rmg.2017.83.3.
Letouzey, J., Kimura, M., 1984. Okinawa Trough genesis: structure and evolution of a backarc basin developed in a continent. Marine and Petroleum Geology 2, 111–130.
Liou, J., Zhang, R., Ernst, W.G., Liu, J., McLimans, R., 1998. Mineral parageneses in the Piampaludo eclogitic body, Gruppo di Voltri, western Ligurian Alps. Schweizerische Mineralogische Und Petrographische Mitteilungen 78 (2), 317–335. https://doi.org/10.5169/seals-59291.
Magni, V., Faccenna, C., van Hunen, J., Funiciello, F., 2014. How collision triggers backarc extension: insight into Mediterranean style of extension from 3-D numerical models. Geology 42 (6), 511–514. https://doi.org/10.1130/G35446.1.
Mantovani, E., Viti, M., Babbucci, D., Tamburelli, C., Albarello, D., 2001. Back arc extension: which driving mechanism? In: Jessell, M. J. 2001. General Contributions: 2001. J. Virtual Explorer 3, 17-44.
Marshak, S., 1988. Kinematics of orocline and arc formation in thin-skinned orogens. Tectonics 7 (1), 73–86. https://doi.org/10.1029/TC007i001p00073.

Massonne, H.-J., Schreyer, W., 1987. Phengite geobarometry based on the limiting assemblage with K-feldspar, phlogopite, and quartz. Contrib. Mineral. Petrol. https://doi.org/10.1007/bf00375235.
Massonne, H.-J., Willner, A.P., 2008. Phase relations and dehydration behaviour of psammopelite and mid-ocean ridge basalt at very-low-grade to low-grade metamorphic conditions. Eur. J. Mineral. 20 (5), 867–879. https://doi.org/10.1127/0935-1221/2008/0020-1871.
Massone, H.-J., Cálderon, M., 2008. P-T evolution of metapelites from the Guarguaraz complex, Argentina: evidence for Devonian crustal thickening close to the western Gondwana margin. Revista Geológica De Chile 35 (2), 215–231. https://doi.org/10.4067/S0716-02082008000200002.
Metcalf, R.V., Shervais, J.W., 2008. Suprasubduction-zone ophiolites: is there really an ophiolite conundrum? In: Wright, J.E., Shervais, J.W. (Eds.), Ophiolites, Arcs, and Batholiths: A Tribute to Cliff Hopson. Geol. Soc. Am. Special Paper 438, 191–222. Doi: 10.1130/2008.2438(07).
Mosquera, A., Ramos, V.A., 2006. Intraplate deformation in the Neuquén Basin. In: Kay, S.M., Ramos, V.A. (Eds.), Evolution of an Andean Margin: A Tectonic and Magmatic View from the Andes to the Neuquén Basin (35°–39°S latitude). Geol. Soc. Am. Special Paper 407, 97–124. DOI: 10.1130/2006.2407(05).
Mullen, E., 1983. MnO/TiO2/P2O5: a minor element discriminant for basaltic rocks of oceanic environments and its implications for petrogenesis. Earth Planet. Sci. Lett. 62 (1), 53–62. https://doi.org/10.1016/0012-821X(83)90070-5.
Muñoz-Montecinos, J., Angiboust, S., Cambeses, A., García-Casco, A., 2020. Multiple veining in a paleo–accretionary wedge: the metamorphic rock record of prograde dehydration and transient high pore-fluid pressures along the subduction interface (Western Series, central Chile). Geosphere 16 (3), 765–786. https://doi.org/10.1130/GES02227.1.
Muñoz-Montecinos, J., Cambeses, A., Angiboust, S., 2024. Accretion and subduction mass transfer processes: Zircon SHRIMP and geochemical insights from the Carboniferous Western Series Central Chile. Int. Geol. Rev. 66 (1), 54–80. https://doi.org/10.1080/00206814.2023.2185822.
Oliveros, V., Vásquez, P., Creixell, C., Lucassen, F., Ducea, M.N., Ciocca, I., González, J., Espinoza, M., Salazar, E., 2020. Lithospheric evolution of the Pre- and Early andean convergent margin Chile. Gondwana Res. 80, 202–227. https://doi.org/10.1016/j.gr.2019.11.002.
Oriolo, S., Schulz, B., González, P.D., Bechis, F., Olaizola, E., Krause, J., Renda, E.M., Vizán, H., 2019. The late Paleozoic tectonometamorphic evolution of Patagonia revisited: insights from the pressure-temperature-deformation-time (P-T-D-t) path of the Gondwanide basement of the North Patagonian Cordillera (Argentina). Tectonics 38, 2378–2400. https://doi.org/10.1029/2018TC005358.
Oriolo, S., González, P.D., Renda, E.M., Basei, M.A.S., Otamendi, J., Cordenons, P., Marcos, P., Yoya, M.B., Justiniano, C.A., Suarez, R., 2023. Linking accretionary orogens with continental crustal growth and stabilization: lessons from Patagonia. Gondwana Res. 121, 368–382. https://doi.org/10.1016/j.gr.2023.05.011.
Palape, C., Quezada, P., Bastías, J., Hervé, F., Reyes, T., Veas, M., Vildoso, F., Calderón, M., Theye, T., Fuentes, F., Chiaradia, M., 2022. Forearc tectonics and volcanism during the Devonian–Carboniferous evolution of the North Patagonian segment, southern Chile (41,3°S). Front. Earth Sci. 10, 873785. https://doi.org/10.3389/feart.2022.873785.
Pankhurst, R.J., Rapela, C.W., Fanning, C., Marquez, M., Márquez, M.J., 2006. Gondwanide continental collision and the origin of Patagonia. Earth Sci. Rev. https://doi.org/10.1016/j.earscirev.2006.02.001.
Pankhurst, R.J., Rapela, C.W., López de Luchi, M.G., Rapalini, A.E., Fanning, C.M., Galindo, C., 2014. The Gondwana connections of northern Patagonia. J. Geol. Soc. 171, 313–328. https://doi.org/10.1144/jgs2013-081.
Peacock, S.M., 1987. Creation and preservation of subduction-related inverted metamorphic gradients. J. Geophys. Res. 92, 763–781. https://doi.org/10.1029/JB092iB12p12763.
Pearce, J.A., 2008. Geochemical fingerprinting of oceanic basalts with applications to ophiolite classification and the search for Archean oceanic crust. Lithos 100 (1–4), 14–48. https://doi.org/10.1016/j.lithos.2007.06.016.
Pearce, J.A., Stern, R.J., Bloomer, S.H., Fryer, P., 2005. Geochemical mapping of the Mariana arc-basin system: implications for the nature and distribution of subduction components. Geochem. Geophys. 6, Q07006. https://doi.org/10.1029/2004GC000895.
Pearce, J.A., Stern, R.J., 2006. Origin of back-arc basin magmas: Trace element and isotope perspectives. In: Christie, D.M., Fisher, C.R., Lee, S.-M., Givens, S. (Eds.), Geophysical Monograph Series, Vol. 166. American Geophysical Union, pp. 63–86. https://doi.org/10.1029/166GM06.
Penniston-Dorland, S.C., Kohn, M.J., Manning, C.E., 2015. The global range of subduction zone thermal structures from exhumed blueschists and eclogites: rocks are hotter than models. Earth Planet. Sci. Lett. 428, 243–254. https://doi.org/10.1016/j.epsl.2015.07.031.
Perchuk, L.L., Aranovich, L.Y., Podlesskii, K.K., Lavrant'Eva, I.V., Gerasimov, V.Y., Fed'Kin, V.V., Kitsul, V.I., Karsakov, L.P., Berdnikov, N.V., 1985. Precambrian granulites of the Aldan shield, eastern Siberia, USSR. J. Metamorph. Geol. 3(3), 265-310. Doi: 10.1111/j.1525-1314.1985.tb00321.x.
Pérez Luján, S.B., Boedo, F.L., Ariza, J.P., Vujovich, G.I., Alvarado, P., Kay, S.M., 2021. The Cuyano proto-ocean between the Chilenia and Cuyania terranes: rifting and plume interaction during the Neoproterozoic –early Palaeozoic evolution of the SW Gondwana margin. Geol. Magazine 158, 1773–1794. https://doi.org/10.1017/S0016756821000303.
Plissart, G., González-Jiménez, J.M., Garrido, L.N.F., Colás, V., Berger, J., Monnier, C., Diot, H., Padrón-Navarta, J.A., 2019. Tectono-metamorphic evolution of subduction channel serpentinites from South-Central Chile. Lithos 336–337, 221–241. https://doi.org/10.1016/j.lithos.2019.03.023.
Ramos, V.A., Jordan, T.E., Allmendinger, R.W., Mpodozis, C., Kay, S.M., Cortés, J.M., Palma, M.A., 1986. Paleozoic terranes of the Central Argentine Chilean Andes. Tectonics 5, 855–880. https://doi.org/10.1029/TC005i006p00855.
Ramos, V.A., 2008. Patagonia: a paleozoic continent adrift? J. South Am. Earth Sci. 26, 235–251. https://doi.org/10.1016/j.jsames.2008.06.002.
Ramos, V.A., 2009. Anatomy and global context of the Andes: main geologic features and the Andean orogenic cycle. In: Kay SM, Ramos VA, Dickinson WR (eds) Backbone of the Americas: shallow subduction, plateau uplift, and ridge and terrane collision. Geol. Soc. Am. Memoir 204, 31–65. DOI: 10.1130/2009.1204(02).
Rapalini, A., López de Luchi, M., Tohver, E., Cawood, P.A., 2013. The south American ancestry of the North Patagonian Massif: geochronological evidence for an autochthonous origin? Terra Nova 24 (3), 337–342. https://doi.org/10.1111/ter.12043.
Rapela, C.W., Pankhurst, R.J., Fanning, C.M., Grecco, L.E., 2003. Basement evolution of the Sierra de la Ventana Fold Belt: new evidence for Cambrian continental rifting along the southern margin of Gondwana. J. Geol. Soc. London 160, 613–628. https://doi.org/10.1144/0016-764902-112.
Rapela, C.W., Pankhurst, R.J., 2020. The continental crust of northeastern Patagonia. Ameghiniana 57 (5), 480–498. https://doi.org/10.5710/AMGH.17.01.2020.3270.
Rapela, C.W., Hervé, F., Pankhurst, R.J., Calderón, M., Fanning, C.M., Quezada, P., Poblete, F., Palape, C., Reyes, T., 2021. The Devonian accretionary orogen of the North Patagonian cordillera. Gondwana Res. 96, 1–21. https://doi.org/10.1016/j.gr.2021.04.004.
Rapela, C.W., García, M., Hervé, F., Pankhurst, R.J., Calderón, M., Fanning, C.M., Verdecchia, S.O., 2024. Late Paleozoic magmatism and foreland deformation associated with opening and closing of marginal basins in the North Patagonian Andes. J. Geol. Soc. London 181. https://doi.org/10.1144/jgs2023-171.
Ravna, K., 2000. The garnet-clinoPrproxene Fe 2+ -Mg geothermometer: an updated calibration: G-C F-M Geothermobarometer Update. J. Metamorph. Geol. 18 (2), 211–219. https://doi.org/10.1046/j.1525-1314.2000.00247.x.
Reagan, M.K., Ishizuka, O., Stern, R.J., Kelley, K.A., Ohara, Y., Blichert-Toft, J., Bloomer, S.H., Cash, J., Fryer, P., Hanan, B.B., Hickey-Vargas, R., Ishii, T., Kimura, J.-I., Peate, D.W., Rowe, M.C., Woods, M., 2010. Fore-arc basalts and subduction initiation in the Izu-Bonin-Mariana system. Geochem. Geophys. 11 (3), Q03X12. https://doi.org/10.1029/2009GC002871.
Riley, T.R., Burton-Johnson, A., Flowerdew, M.J., Poblete, F., Castillo, P., Hervé, F., Leat, P.T., Millar, I.L., Bastias, J., Whitehouse, M.J., 2023. Palaeozoic–Early Mesozoic geological history of the Antarctic Peninsula and correlations with Patagonia: Kinematic reconstructions of the proto-Pacific margin of Gondwana. Earth Sci. Rev. 236, 104265. https://doi.org/10.1016/j.earscirev.2022.104265.
Ritter, S., Balázs, A., Ribeiro, J., Gerya, T., 2024. Magmatic fingerprints of subduction initiation and mature subduction: numerical modelling and observations from the Izu-Bonin-Mariana system. Front. Earth Sci. 12, 1286468. https://doi.org/10.3389/feart.2024.1286468.
Romero, R., González-Jiménez, J.M., Barra, F., Leisen, M., Garrido, L.N., Talavera, C., Gain, S.E.M., Griffin, W.L., O'Reilly, S.Y., Reich, M., Morata, D., 2017. Timing the tectonic mingling of ultramafic rocks and metasediments in the southern section of the coastal accretionary complex of central Chile. Int. Geol. Rev. 60 (16), 2031–2045. https://doi.org/10.1080/00206814.2017.1402377.
Romero, R., Barra, F., Leisen, M., Salazar, E., González-Jiménez, J.M., Reich, M., 2019. Sedimentary provenance of the late Paleozoic metamorphic basement, south-central Chile: implications for the evolution of the western margin of Gondwana. Int. Geol. Rev. 62 (5), 598–613. https://doi.org/10.1080/00206814.2019.1627589.
Schellart, W.P., Freeman, J., Stegman, D.R., Moresi, L., May, D., 2007. Evolution and diversity of subduction zones controlled by slab width. Nature 446, 308–311. https://doi.org/10.1038/nature05615.
Schilling, M.E., Carlson, R.W., Tassara, A., Conceição, R.V., Bertotto, G.W., Vásquez, M., Muñoz, D., Jalowitzki, T., Gervasoni, F., Morata, D., 2017. The origin of Patagonia revealed by Re-Os systematics of mantle xenoliths. Precambr. Res. 294, 15–32. https://doi.org/10.1016/j.precamres.2017.03.008.
Shervais, J.W., 1982. Ti-V plots and the petrogenesis of modern and ophiolite lavas. Earth and Planet. Sci. Lett. 59, 101–118. https://doi.org/10.1016/0012-821X(82)90120-0.
Sibuet, J.C., Hsu, S.K., 2004. How was Taiwan created? Tectonophysics 379, 159–181. https://doi.org/10.1016/j.tecto.2003.10.022.
Stern, R.J., Gerya, T., 2018. Subduction initiation in nature and models: a review. Tectonophysics 746, 173–198. https://doi.org/10.1016/j.tecto.2017.10.014.
Sun, S.S., McDonough, W.F., 1989. Chemical and isotopic systematics of oceanicbasalts: implications for mantle composition and processes. Geol. Soc. Lond. Special Publications 42, 313–345. https://doi.org/10.1144/GSL.SP.1989.042.01.19.
Tapponnier, P., 1977. Evolution tectonique du système alpin en Méditerranée: poinçonnement et écrasement rigide-plastique. Bull. Soc. Geol. Fr. 7 (3), 437–460. https://doi.org/10.2113/gssgfbull.S7-XIX.3.437.
Thomas, W.A., Astini, R.A., 2003. Ordovician accretion of the Argentine Precordillera terrane to Gondwana: a review. J. South Am. Earth Sci. 16, 67–79. https://doi.org/10.1016/S0895-9811(03)00019-1.
Torsvik, T.H., Cocks, L.R.M., 2013. Gondwana from top to base in space and time. Gondwana Res. 24, 999–1030. https://doi.org/10.1016/j.gr.2013.06.012.
Uriz, N.J., Cingolani, C.A., Taboada, A.C., Arnol, J.A., Stipp Basei, M.A., Abre, P., Coehlo dos Santos, G.S., 2022. Provenance of pre- and Carboniferous sequences of the Esquel-Arroyo Pescado-Tepuel regions (Argentine Patagonia): a combined U–Pb and Hf isotope study of detrital zircon and constraints on depositional setting. J. South Am. Earth Sci. 119, 103953. https://doi.org/10.1016/j.jsames.2022.103953.
Wallace, L.M., McCaffrey, R., Beavan, J., Ellis, S., 2005. Rapid microplate rotations and back-arc rifting at the transition between collision and subduction. Geology 33, 857–860. https://doi.org/10.1130/G21834.1.

Wallace, L.M., Ellis, S., Mann, P., 2009. Collisional model for rapid fore-arc block rotations, arc curvature, and episodic back-arc rifting in subduction settings. Geochem. Geophys. 10, Q05001. https://doi.org/10.1029/2008GC002220.

Warr, L.N., 2021. IMA–CNMNC approved mineral symbols. Mineral. Mag. 85 (3), 291–320. https://doi.org/10.1180/mgm.2021.43.

Willner, A.P., 2005. Pressure–temperature evolution of a late palaeozoic paired metamorphic belt in North–Central Chile (34°–35°30′S). J. Petrol. 46 (9), 1805–1833. https://doi.org/10.1093/petrology/egi035.

Willner, A.P., Glodny, J., Gerya, T.V., Godoy, E., Massonne, H.-J., 2004. A counterclockwise PTt path of high-pressure/low-temperature rocks from the Coastal Cordillera accretionary complex of south-central Chile: Constraints for the earliest stage of subduction mass flow. Lithos 75, 283–310. https://doi.org/10.1016/j.lithos.2004.03.002.

Willner, A.P., Thomson, S.N., Kröner, A., Wartho, J., Wijbrans, J.R., Hervé, F., 2005. Time markers for the evolution and exhumation history of a late palaeozoic paired metamorphic belt in North–Central Chile (34°–35°30′S). J. Petrol. 46 (9), 1835–1858. https://doi.org/10.1093/petrology/egi036.

Willner, A.P., Gerdes, A., Massonne, H.-J., Schmidt, A., Sudo, M., Thomson, S.N., Vujovich, G.I., 2011. The geodynamics of collision of a microplate (Chilenia) in Devonian times deduced by the pressure-temperature-time evolution within part of a collisional belt (Guarguaraz Complex, W-Argentina). Contrib. Mineral. Petrol. Doi: 10.1007/s00410-010-0598-8.

Winchester, J.A., Floyd, P.A., 1977. Geochemical discrimination of different magma series and their differentiation products using immobile elements. Chem. Geol. 20, 325–343. https://doi.org/10.1016/0009-2541(77)90057-2.